ACOUSTIC RIDGE WAVEGUIDE TECHNOLOGY

Robert S. Wagers

Texas Instruments Incorporated

August 1976

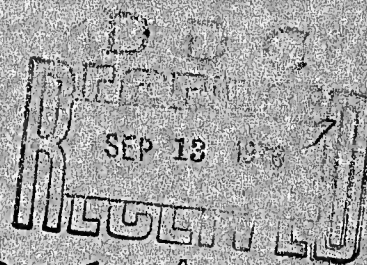Final Technical Report
6 January 1975 - 30 June 1976

Sponsored by
Advanced Research Projects Agency
ARPA Order No. 2827

The views and conclusions contained in this document are those of the authors and should not be interpreted as necessarily representing the official policies, either expressed or implied, of the Advanced Research Projects Agency or the U. S. Government.

ACOUSTIC RIDGE WAVEGUIDE TECHNOLOGY

Contract No. N00014-75-C-0317

Robert S. Wagers

Texas Instruments Incorporated

August 1976

Final Technical Report
6 January 1975 - 30 June 1976

Sponsored by
Advanced Research Projects Agency
ARPA Order No. 2827

REPORT DOCUMENTATION PAGE	READ INSTRUCTIONS BEFORE COMPLETING FORM

1. REPORT NUMBER	2. GOVT ACCESSION NO.	3. RECIPIENT'S CATALOG NUMBER

4. TITLE (and Subtitle)	5. TYPE OF REPORT & PERIOD COVERED
ACOUSTIC RIDGE WAVEGUIDE TECHNOLOGY	Final Technical Report, 6 January 1975-30 June 1976
	6. PERFORMING ORG. REPORT NUMBER
	08-76-41

7. AUTHOR(s)	8. CONTRACT OR GRANT NUMBER(s)
Robert S. Wagers	N00014-75-C-0317 ARPA Order 2827

9. PERFORMING ORGANIZATION NAME AND ADDRESS	10. PROGRAM ELEMENT, PROJECT, TASK AREA & WORK UNIT NUMBERS
Texas Instruments Incorporated Central Research Laboratories P. O. Box 5936 Dallas, Texas 75222	ARPA Order No. 2827 Program Code No. 5D10

11. CONTROLLING OFFICE NAME AND ADDRESS	12. REPORT DATE
Advanced Research Projects Agency 1400 Wilson Boulevard Arlington, Virginia 22209	August 1976
	13. NUMBER OF PAGES
	83

14. MONITORING AGENCY NAME & ADDRESS(if different from Controlling Office)	15. SECURITY CLASS. (of this report)
Office of Naval Research 800 North Quincy Street Arlington, Virginia 22217	Unclassified
	15a. DECLASSIFICATION/DOWNGRADING SCHEDULE

16. DISTRIBUTION STATEMENT (of this Report)

17. DISTRIBUTION STATEMENT (of the abstract entered in Block 20, if different from Report)

18. SUPPLEMENTARY NOTES

19. KEY WORDS (Continue on reverse side if necessary and identify by block number)

Surface acoustic waves	Lithium niobate
Acoustic	Quartz
Ultrasonic	Transducers
Waveguide	Filters
Orientation dependent etching	Variational

20. ABSTRACT (Continue on reverse side if necessary and identify by block number)

The feasibility of etching single-crystal lithium niobate and α-quartz to produce wedge-shaped acoustic waveguides has been examined. The primary etchant considered was boiling hydrofluoric acid. Etch masks of sputtered chrome/gold were employed. Highly uniform small (~ 0.001 inch high) waveguides could be produced in quartz substrates. $LiNbO_3$ waveguide fabrication was not possible due to the high defect density in the material. Spurious mode excitation problems were examined and found to be minimal in unapodized →over

DD FORM 1473 EDITION OF 1 NOV 65 IS OBSOLETE

transducers on mechanically lapped waveguides with large transverse dimensions. Smaller transverse dimensions or apodization of the transducers introduced interfering modes. Apodization of interdigitated transducers on wedge waveguides was evaluated as a means of achieving bandpass shaping. The entire coupling range was found to be controlled by the first wavelength of apodization. Thus, impulse response weighting by apodization will require control of electrode geometry to within fractions of a wavelength from the apex of the waveguide.

TECHNICAL REPORT SUMMARY

The feasibility of fabricating acoustic wedge waveguides and associated interdigital transducers has been examined. The method of waveguide formation considered was orientation-dependent etching of single crystal lithium niobate (LiNbO$_3$) and α-quartz.

A primary motivation for developing acoustic waveguides is to take advantage of the potential size reduction over current surface acoustic wave technology. Waveguide components represent the next step in microminiaturization of acoustic signal processing devices. Devices that may be developed include directional couplers, ring resonators, and serial memory. In addition, because of the high degree of spatial confinement of the acoustic energy, nonlinear and acousto-optic interactions become possible.

The technical problems associated with this research are threefold: (1) development of suitable etching processes for waveguide formation, (2) development of fine geometry stencils for transducer fabrication, and (3) characterization of transducer weighting procedures for bandpass shaping.

- ## Waveguide Formation

The etching process employed during this work required boiling the crystals of LiNbO$_3$ and quartz in hydrofluoric acid. The substrates were masked off with sputtered films of chromium and gold and then etched in boiling hydrofluoric acid. We found, however, that erosion of the chromium-quartz interface occurred at a sufficiently fast and uncontrollable rate to prevent fabrication of large-dimension waveguides. In addition, the long etch times employed revealed crystal defects in the quartz substrates. These defects had the appearance of cylindrical voids that originated at the seed of the boule and were maintained during crystal growth. Consequently, wafers sliced from the boule had these voids piercing them. Because the diameters of the voids were quite small, etch times of one to three hours were required to reveal them.

$LiNbO_3$ presented even worse crystal defect problems than did quartz. The defect density was so great that the longest propagation length between defects measured in the tens of mils. Erosion of the chrome/gold etch mask on $LiNbO_3$ was not a problem after a rigorous SYTON polishing procedure was adopted.

The major conclusions reached after this investigation are:

1. Orientation-dependent etching of quartz by boiling HF to produce small geometry waveguides ($\sim$ 0.001 inch high) can be accomplished with high waveguide uniformity.

2. Orientation-dependent etching of quartz by boiling HF to produce larger geometry waveguides ($\sim$ 0.003 inch high) can be limited by line defects which emanate from the seed of the boule and pierce the wafers cut from the boule.

3. Orientation-dependent etching of quartz by boiling HF to produce still larger geometry waveguides (> 0.003 inch high) is not currently possible due to the high rate of etch mask erosion. (The etch mask was sputtered chrome and gold. The quartz wafers were SYTON polished.)

4. Orientation-dependent etching of $LiNbO_3$ by boiling HF is not a sufficiently controllable process due to the defects inherent in even the best $LiNbO_3$ available.

● Transducer Fabrication

No substantive results on stencil fabrication or on application to transducer definition were obtained due to the major difficulties encountered in waveguide etching.

● Transducer Weighting Characterization

In the work reported here we concentrated on the sensitivity of the transducers' electrical characteristics to variations in the metallization

produced. As might be expected from the fact that the transducers are very small (essentially a collection of end-effects), the sensitivity we observed was considerable. Apodization of interdigital transducers as a means of band-pass weighting was examined for sensitivity to fabrication errors. The results showed that the coupling dropped off so rapidly with apodization that, in only $1/2 \lambda$ of electrode length variation, the coupling could be varied from 100% to only 40% of full coupling. Apodization is thus such a sensitive process that at 40 MHz, where $\lambda \sim 0.002$ inch, it is questionable whether it can be applied, even using stencils.

No special equipment has been purchased or developed on this contract.

TABLE OF CONTENTS

TABLE OF CONTENTS
(continued)

LIST OF TABLES

LIST OF ILLUSTRATIONS

SECTION I

INTRODUCTION

Acoustic ridge waveguides have been examined by a number of investigators[1-5] over the past several years. Most of this work has centered on rectangular-profiled ridges on a substrate, with only a small effort[2] devoted to triangular or wedge-shaped waveguides. While some of these investigations have met with laboratory successes, a general interest in acoustic waveguide components has lagged, principally because (1) extremely difficult fabrication procedures are required for the production of a waveguide, and (2) the frequency limitations imposed by the fabrication abilities make the waveguide components inferior to other signal processing device alternatives.

Because this technology has been fundamentally limited by fabrication ability, we have examined the possibility of producing waveguides by orientation-dependent etching (ODE) of single crystal piezoelectric materials. This approach has the potential to extend upward the low operating frequency constraint of these waveguides by a more precise control over waveguide geometry and defect size, since the geometry is defined by photoresist edges and crystal lattice planes. The two materials considered were lithium niobate ($LiNbO_3$) and α-quartz (quartz). The etchant generally employed was boiling hydrofluoric acid (HF), although a few other etchants were considered for quartz.

In addition, on low frequency (1 to 2 MHz) mechanically lapped prototype waveguides we have examined the impedance properties of interdigital transducers. An approximate solution to the problem was obtained analytically, and experimental results were measured for a number of apodized transducers.

The major conclusions reached after this investigation are:

- Orientation-dependent etching of $LiNbO_3$ by boiling HF is not a sufficiently controllable process due to the defects inherent in even the best available $LiNbO_3$.

1

● Orientation-dependent etching of quartz by boiling HF to produce small geometry waveguides (∿ 0.001 inch high) can be accomplished with high waveguide uniformity.

● Orientation-dependent etching of quartz by boiling HF to produce larger geometry waveguides (∿ 0.003 inch high) can be limited by line defects which emanate from the seed of the boule and pierce the wafers cut from the boule.

● Orientation-dependent etching of quartz by boiling HF to produce still larger geometry waveguides (> 0.003 inch high) is not currently possible due to the high rate of etch mask erosion. (The etch mask was sputtered chrome and gold. The quartz wafers were SYTON polished.)

● Interdigital transducer coupling to the waveguide mode is more strongly dependent on electrode end effects than expected. Consequently, transducer weighting by apodization is highly sensitive to fabrication tolerances.

A. Applications

A primary motivation for developing acoustic waveguides is to take advantage of the potential size reduction from current surface acoustic wave (SAW) technology and thus permit the same signal processing functions that are accomplished with SAW devices to be carried out with smaller (and potentially cheaper) waveguide components. In addition, because of the high degree of spatial confinement of the acoustic energy, nonlinear and acousto-optic interactions become possible. Devices that may eventually be developed include directional couplers, ring resonators, and serial memories.

B. Approach to Waveguide Development

The basic configuration under development is shown in Figure 1. This configuration was chosen over other alternatives for two principal reasons: (1) the fundamental mode of the ideal structure is dispersionless; and (2) when

2
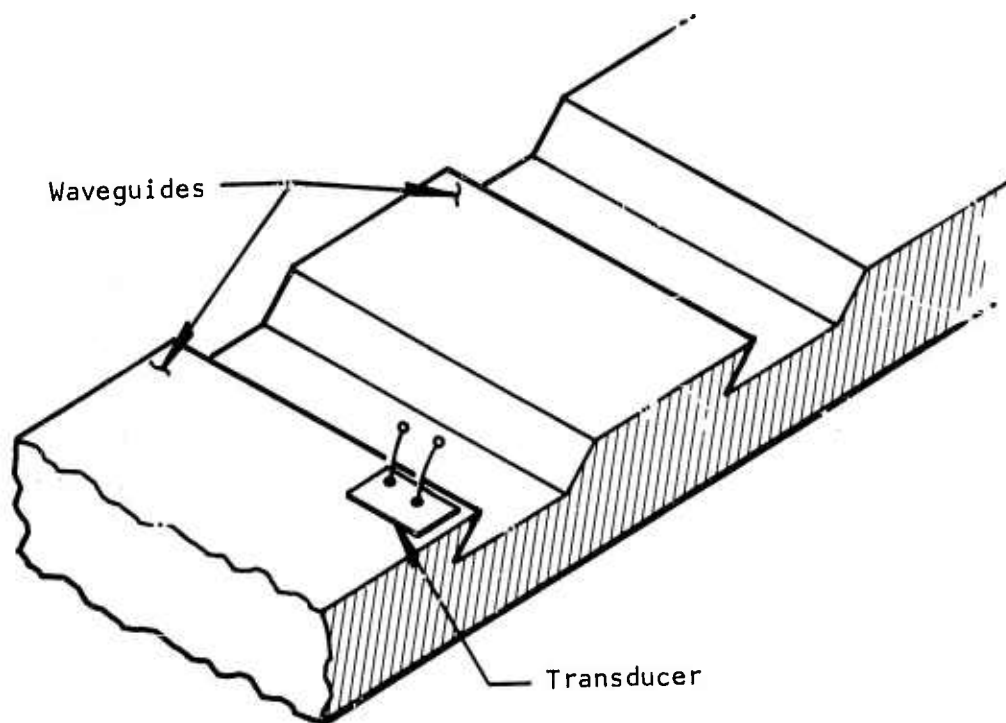
Figure 1 Acoustic Waveguides on a Piezoelectric Wafer.
The overhanging wedge-shaped structures confine
and guide the wave. Transducers are fabricated
on the face of the waveguide that is coplanar
with the top surface of the wafer.

3

the structure is fabricated on a wafer as shown, the flexure and electric potential of the guide are compatible with transducer fabrication in the plane of the wafer's top surface. Development of a delay line with the configuration of Figure 1 involves two major tasks, fabrication of the waveguide and fabrication of the transducers.

1. Waveguide Fabrication

Orientation-dependent etching of crystals has been demonstrated in many materials. Silicon exhibits preferential etching, and a vast body of literature has been produced dealing with ODE of silicon. Unfortunately, silicon is not piezoelectric, and while waveguides may be easily formed[4] in the material, transduction is an exceedingly difficult problem.

Quartz and LiNbO$_3$ also permit preferential etching. While no body of literature on ODE of these two materials exists, Texas Instruments, through the prior work of Dr. D. F. Weirauch,[6] has developed considerable expertise in etching device geometries in quartz and LiNbO$_3$. It is this ODE capability that enables us to consider the configuration of Figure 1. The work on ODE of LiNbO$_3$ and quartz supported by this contract is discussed in Section III.

2. Transducer Fabrication

Optimal transducer design not only includes defining a process that produces coupling metallizations on the waveguides, but also takes into account spurious mode discrimination, fundamental mode impedance matching considerations, sensitivity to photoresist variations, and the ability to accurately weight the transducer structure to achieve a desired frequency response. Work directed toward obtaining guidelines with regard to these problems has been done in parallel with the etching activities. The transducer work has been carried out on low frequency prototype devices that were mechanically cut and polished. This work is discussed in Section II.

4

SECTION II

PROTOTYPE DEVICE STUDIES

A. Introduction

Mechanically lapped prototype acoustic waveguides were built to evaluate spurious mode excitation problems, sensitivity of transducer characteristics to fabrication processing variations, and transducer weighting control. Early work on ID transducer excitation of the waveguides showed that spurious modes excited by the transducer pads could be excessively strong in comparison to the waveguide mode; thus, schemes were sought to decrease their coupling. Transducer weighting and parameter-dependent processing variation were areas in which difficulty was anticipated because the usable electric field of the waveguide mode is confined to within a few wavelengths of the waveguide tip, requiring that electrical coupling be accomplished through the fringing fields at the ends of the electrodes.

B. Transducer Configuration

1. Spurious Delay Line Signals

Schematic representations of the transducers tried for excitation of the waveguides are shown in Figure 2. Figure 2(a) shows a grating mode config- uration with a ground plane on the lower surface of the waveguide. Figures 2(b) and 2(c) illustrate interdigital transducers. For our early experiments on lapped ceramic waveguides all three of the configurations illustrated were considered. In both the Figure 2(a) and 2(b) configurations, where the pads of the transducer were directly on the surface of the crystal, the spurious mode excitation problem was considerable. Consequently, the pads of the transducer were spaced away from the piezoelectric, as shown in Figure 2(c). On the ceramic waveguides this resulted in extremely clean single mode excitation.

(a)

(b)
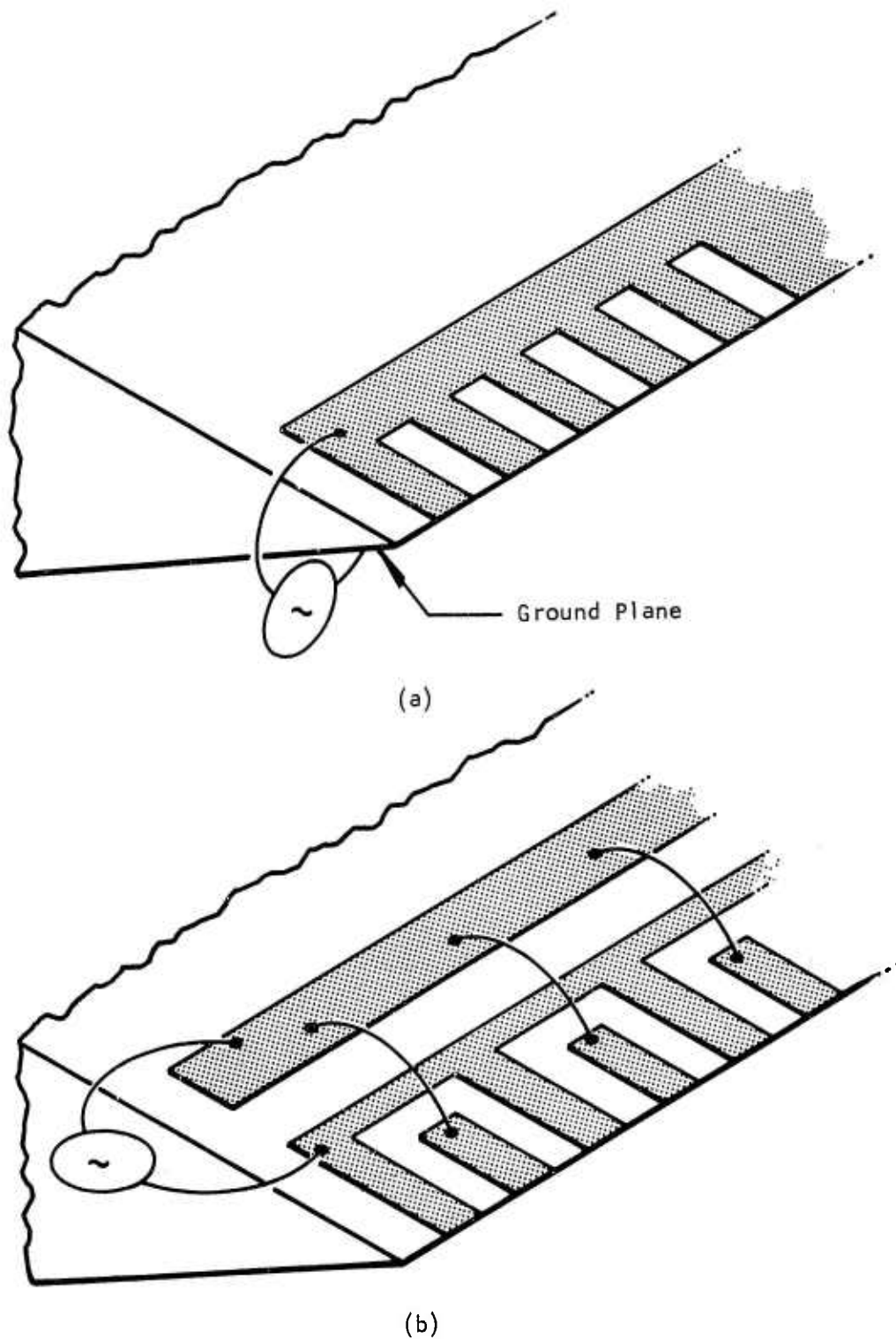
Figure 2   Transducer Configurations Used in the Prototype Device
Evaluation.   Figure 2 (a) shows a grating mode transducer
employing a ground plane.   Figure 2(b) shows an inter-
digital transducer with half the fingers stitch-bonded
to one pad.

Insulating
Nonpiezoelectric
Material
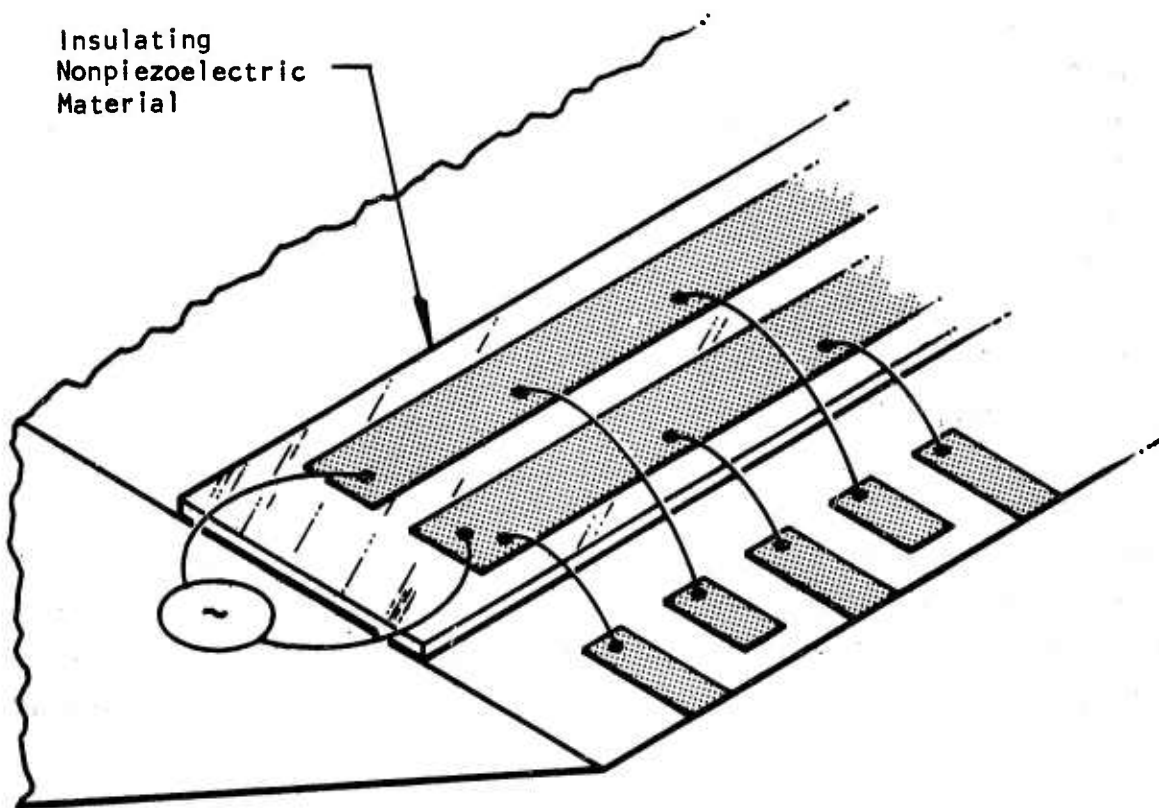
(c)

Figure 2 (continued)   Transducer Configurations Used in the
Prototype Device Evaluation.   In
Figure 2(c) the pads are spaced away
from the ceramic surface, and all fingers
are bonded to the pads.

7

The ceramic waveguides were fabricated from Glennite G-1408. Since this material is similar to PZT-4, we used the already published[7] dispersion and coupling data shown in Figure 3 in evaluating our results. (The specifications supplied for the Glennite ceramic were not sufficiently complete to permit dispersion and coupling calculations.) Top angles of all the ceramic waveguides were about 33°, and the lateral surfaces of 0.75 inch and 0.89 inch were polished until porosity of the material was the factor limiting surface quality. Approximately 3.5 inches of free propagation path was available, and on the tested units, apex roughness throughout the propagation path was less than 0.04 wavelength (0.04 λ) peak-to-peak.

The transducers were 9.5 λ long with equal-width stripes and spaces. They had a uniform overlap and were approximately one-half wavelength wide, i.e., the stripes extended one-half wavelength away from the apex. The wavelength was 0.040 inch. The free propagation distance between the last electrode of the input transducer and the first electrode of the output transducer was 1.0 inch.

Figure 4 shows the insertion loss of a ceramic waveguide in a 50 Ω system. Two modes are clearly visible. The mode at 1 MHz is the lowest order antisymmetric flexural mode, while the mode at about 1.7 MHz is the first higher-order mode. The phase velocities of these modes are indicated by circles in Figure 3. The deep rejection at the transmission zeros of the fundamental mode illustrated in Figure 4 shows how thoroughly the acoustic crosstalk is absent from the device. With insertion to the peak of the first mode at about -35 dB, the average acoustic background level shown is around -90 dB.

2. Ceramic Waveguide Dispersion

Assuming that the transducer fingers are aligned perpendicular to the propagation direction, the transmission zero data of Figure 4 can be used to
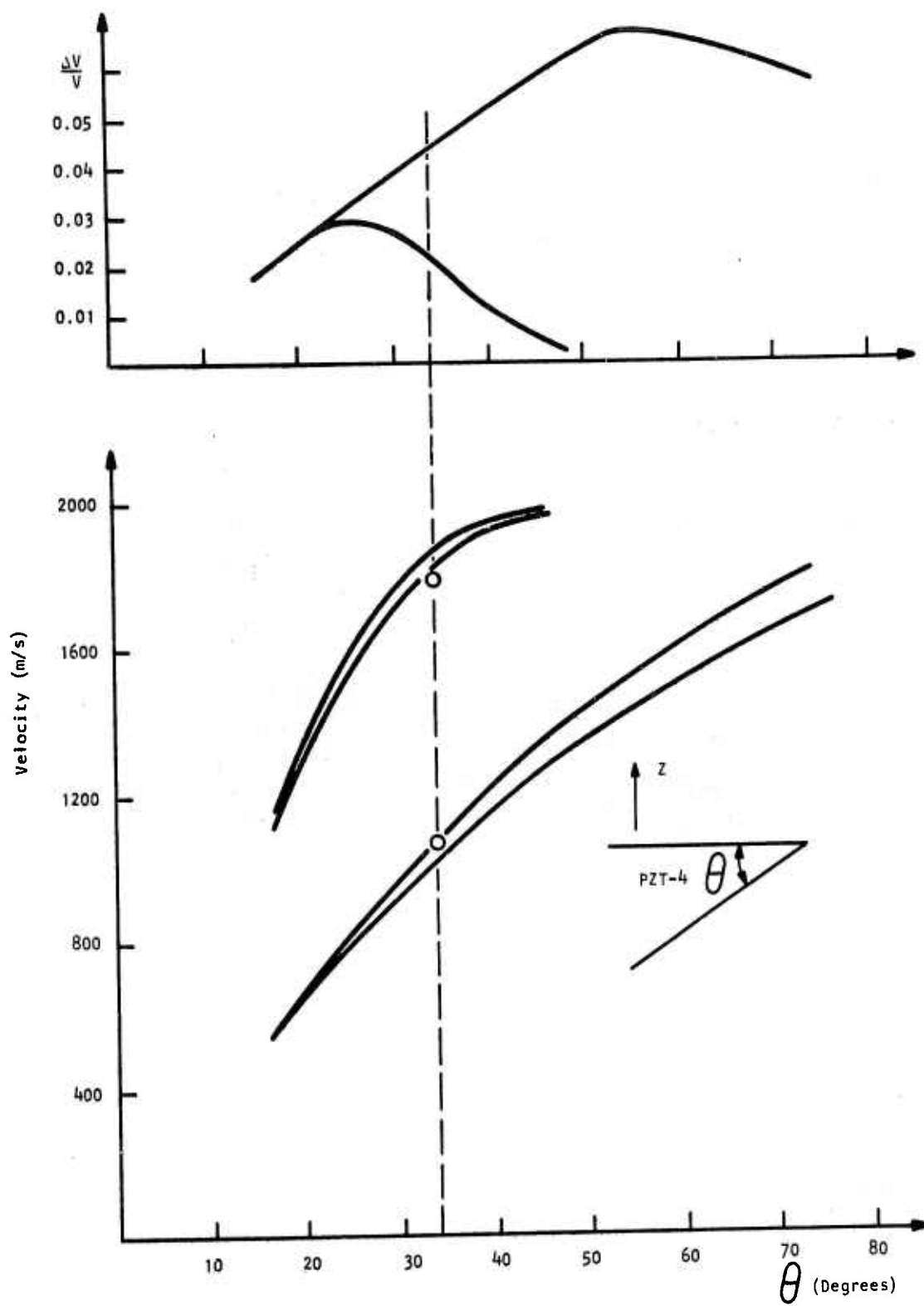
Figure 3 Phase Velocity and Coupling for PZT-4 (from Lagasse[7])

~ -35 dB

10 dB/Div

1.0 MHz   1.6 MHz

200 kHz/Div
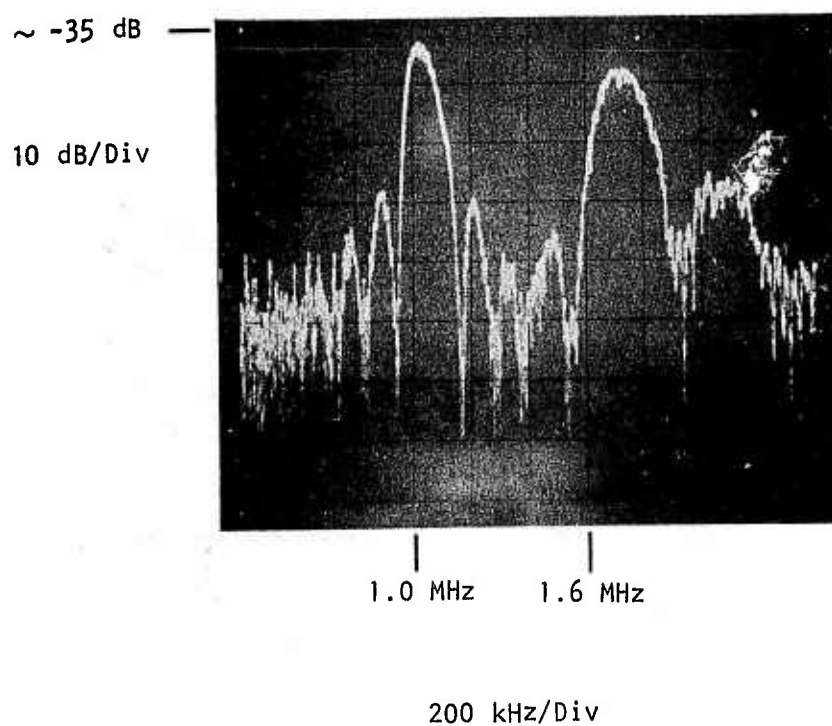
Figure 4   Untuned Insertion Loss of a 33° Ceramic Waveguide.   The transducer
in Figure 2(c) was used in the delay line.

obtain information about the dispersion of the modes. The frequencies of the zeros of transmission of the two modes were counted and combined with the corresponding Fourier wavelengths of the transducer potential to give the dispersion relations shown in Figure 5. There are insufficient data to provide conclusions about the second mode, but the trend for the first mode seems clear. It suggests that over a 47% bandwidth the dispersion is 2.4%.

3. Ceramic Waveguide Impedance

The transducer shown in Figure 2(c) had 0.010 inch lines and spaces, and the electrodes were approximately $\lambda/2$ long (0.020 inch). Only 9.5 λ of interaction was used, so the static reactance of the transducer was quite large. Low frequency measurements indicated a capacitance of 74 pF, giving a reactance of 2.2 kΩ at 1 MHz. To obtain a Smith chart display of the impedance, the transducer was series-tuned with a 340 μH inductor. The result is shown in Figure 6(a). The loop in the impedance display shows clearly and crosses the real axis at midband with a value of $\sim$ 700 Ω. Minor loops on the main lobe are also evident and are a consequence of reflections from the other transducer, which was not waxed during the measurement.

Insertion loss data for the delay line are shown in Figure 7. The upper photo shows rejection of the second mode due to the series tuning. The fundamental mode has an average insertion loss across the passband on the order of -17 dB. A high degree of interference shows in the lower trace, where the amplitude peak-to-peak is greater than 10 dB. This is a consequence of the high impedances of the transducers, which were series-tuned by an inductor; when they were connected to a 50 Ω spectrum analyzer, triple-transit reflections were quite large.

Another surprising characteristic of the frequency response is the very steep skirts on the main passband. These, too, are a consequence of impedance effects. Referring to Figure 6(a) again, one can see that the best

11
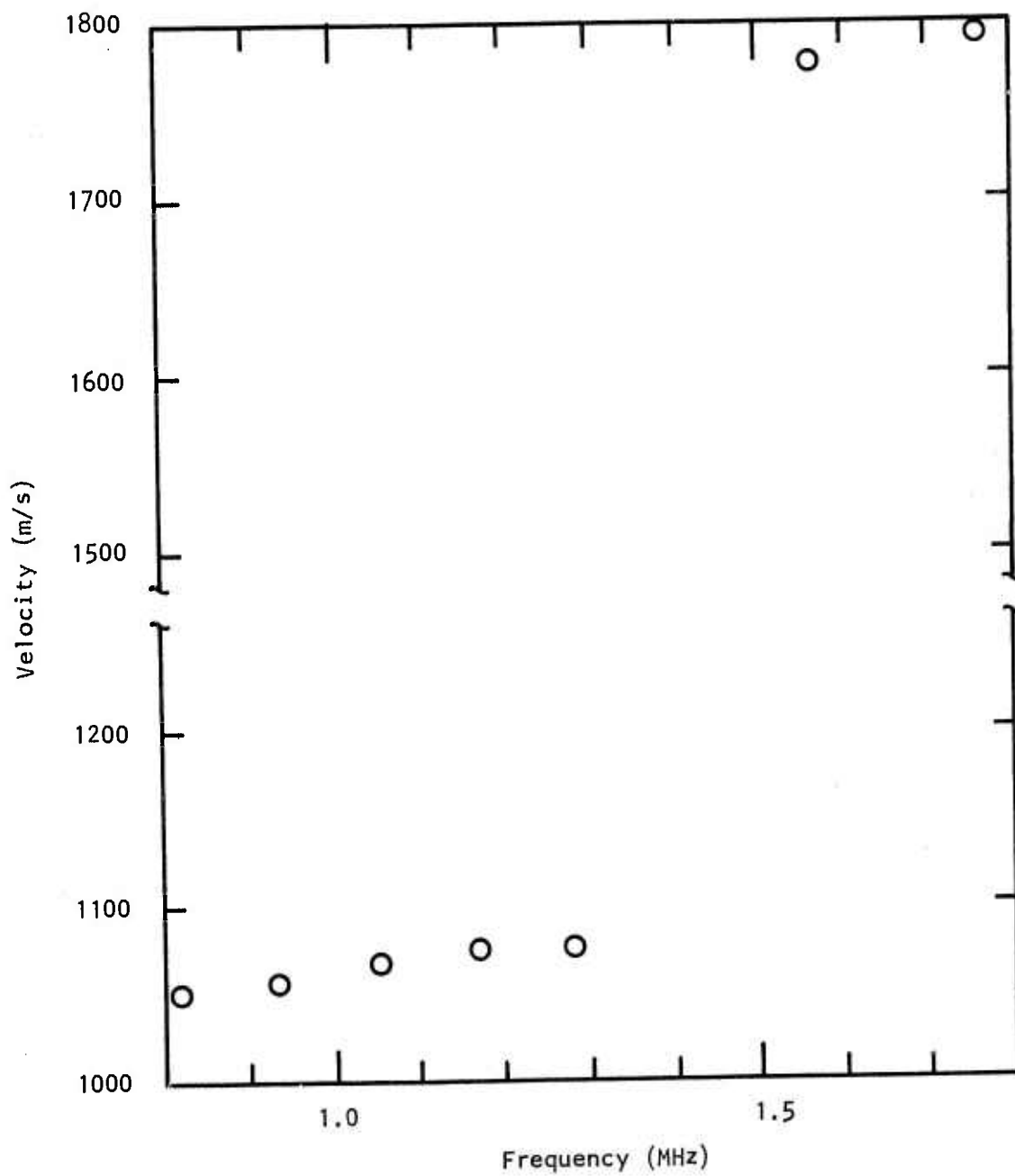
Figure 5   Dispersion Data for the Ceramic Waveguide Shown
in Figures 2(c) and 4.   The transducer has a
0.040 inch wavelength.
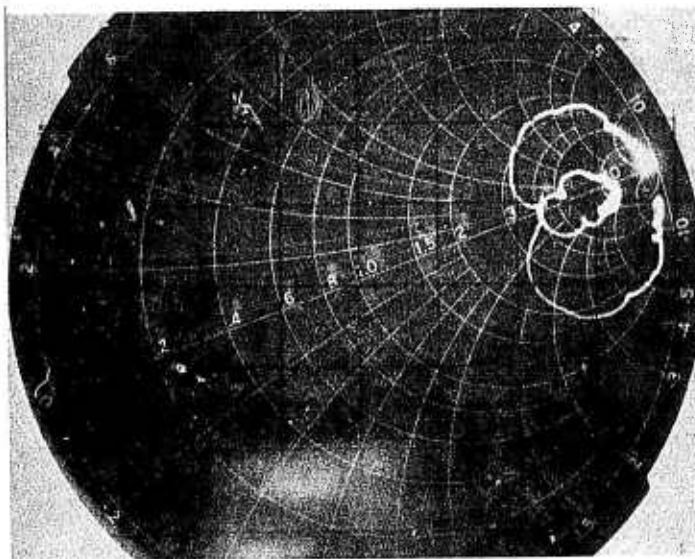
(a)
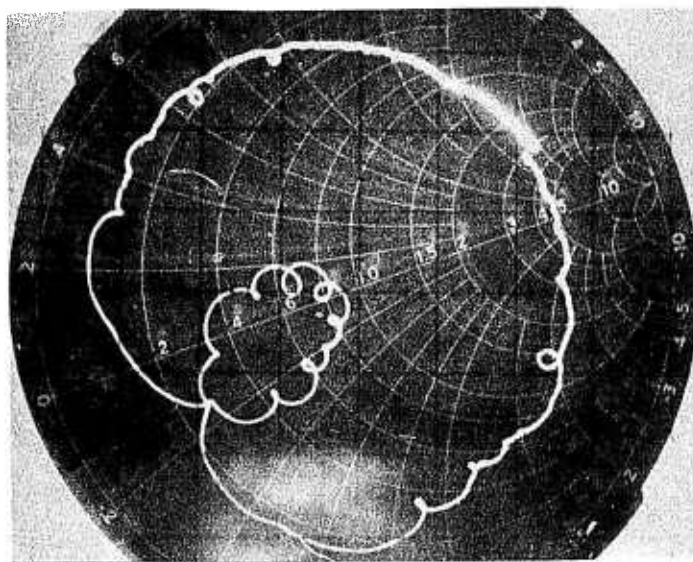
(b)

Figure 6   (a) Impedance of the Transducer After Tuning with a Series
Inductor.   (b) Impedance Looking into a 16:1 Impedance
Transformer in Front of the Series-Tuned Transducer

0 dB

10 dB/Div

(a)

0 dB

10 dB/Div

(b)
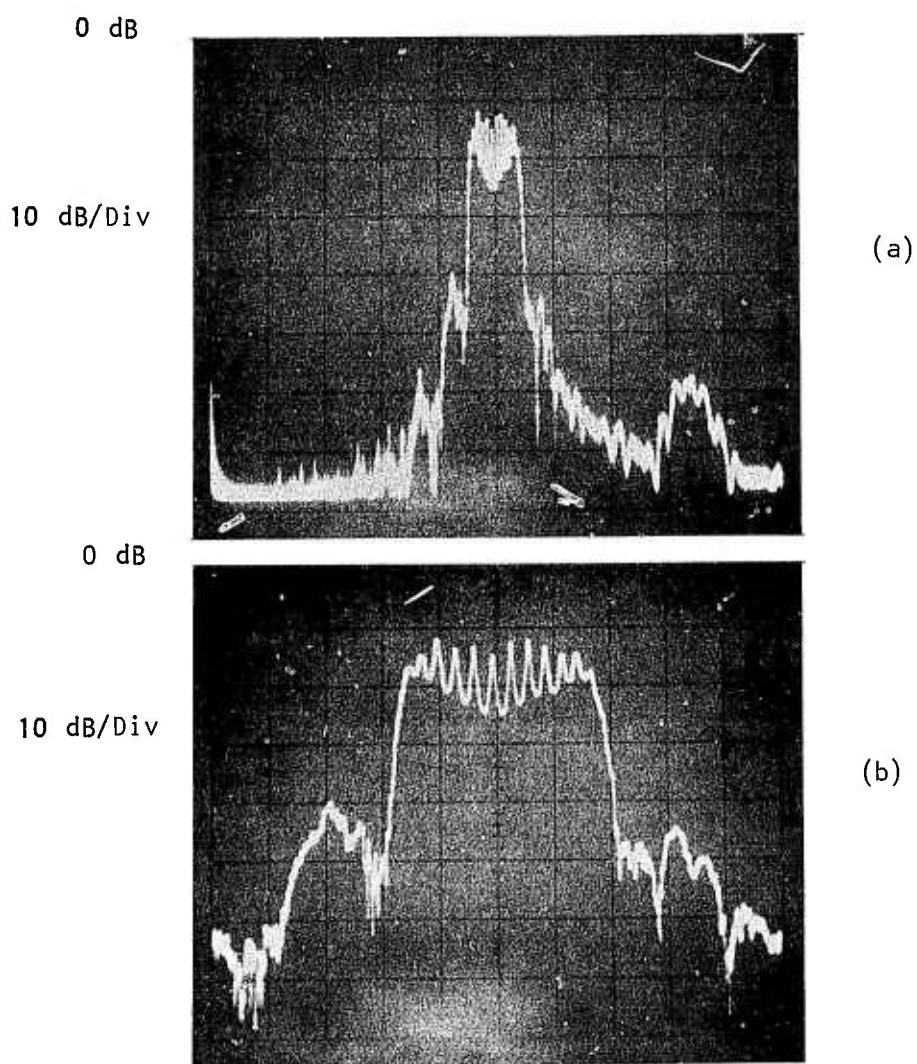
Figure 7   Insertion Losses for the Series-Tuned Waveguide.
(a) 200 kHz/Div; (b) 50 kHz/Div.

14

impedance match for the fundamental mode occurs at the edges of the passband and that at midband, the impedance match is very poor. These mismatching effects serve to steepen the rejection on the passband skirts.

4. Ceramic Waveguide Matching

To overcome the significant impedance mismatch of the waveguide in a 50 Ω system, transformers were added to the matching networks of the transducers. Relcom BT-9 16:1 impedance transformers were placed in front of the already series-tuned transducers. Insertion loss characteristics from the input transformer to the output transformer are shown in Figure 8.

The average insertion loss shown is -10 dB in the passband, and the triple transit ripple is now only 3 dB peak-to-peak. In addition, the steep rejection skirts that were on the sides of the main passband now roll off smoothly. Smith chart characteristics looking into a transformer are shown in Figure 6(b). At midband the real part of the impedance reaches a value of 45 Ω, a considerable improvement over the condition shown in Figure 6(a), where the midband value is $\sim$ 700 Ω. Figure 6(b) also shows there is a strong residual acoustic generation level out-of-band of the fundamental waveguide mode. This level shows up in Figure 8(a) as a pedestal of interference at the -55 dB level.

C. Effect of Insufficient Waveguide Height Above Substrate

One of the principal reasons for examining the wedge-shaped waveguides is that for infinitely large guides the modes are nondispersive. However, in practice, one would like to have the waveguides etched into the substrate as shown in Figure 1 to the shallowest distance possible. Obviously, a trade-off between device performance and processing difficulty must be made.

15

0 dB

10 dB/Div

(a)

0 dB

10 dB/Div

(b)
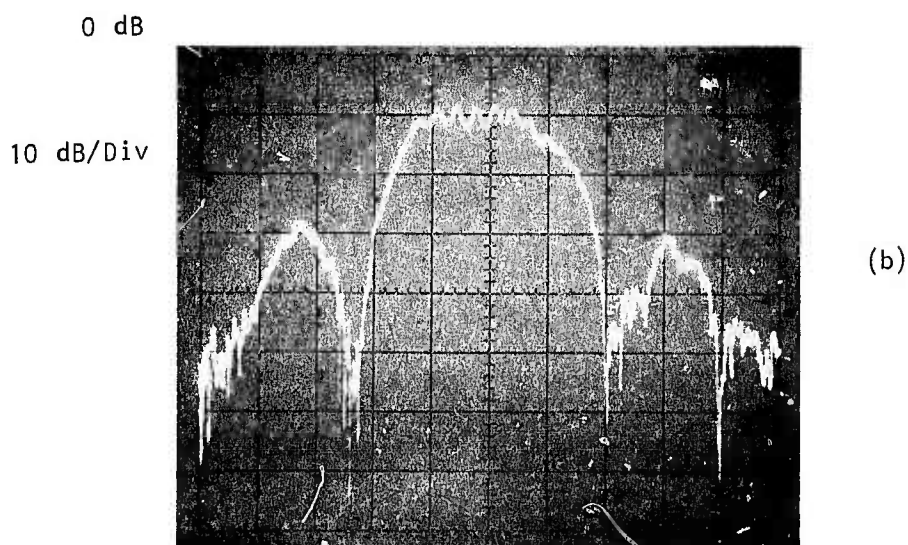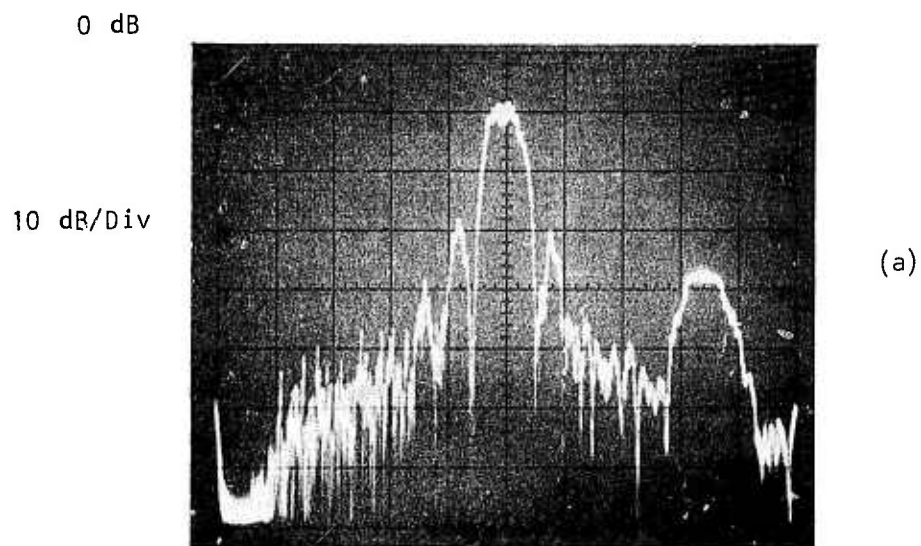
Figure 8   Insertion Losses for the Matched Waveguide.
(a) 200 kHz/Div; (b) 50 kHz/Div.

16

As the wedge dimensions become comparable to a wavelength, the fundamental mode becomes dispersive. For the geometry of Figure 1 the addition of dispersion to the existing modes may be the only consequence of smaller geometry. In other cases, such as that shown in Figure 9(b), where the waveguide is formed on the edge of a plate, other modes may occur. This problem is illustrated by the following experiment.

In the original analysis a model of an infinitely large waveguide, Figure 9(a), was used. The wedge shown is 6 λ from apex to attachment face. For the tightly confined wedgeguide modes this is sufficient to prevent the introduction of dispersion by the attachment face. The waveguide in Figure 9(a) has its two lowest modes at 2288.0 m/s and 3394.4 m/s. For the experiment a 1.25 λ thick Y-cut LiNbO$_3$ plate was cut along the X-axis to produce a waveguide as shown in Figure 9(b). This waveguide has a considerably more complex mode structure than would be indicated by the calculations for Figure 9(a).

Figure 10 shows the untuned frequency response for the Figure 9(b) waveguide when excited by λ = 0.040 inch, N = 9.5, unapodized, one wavelength aperture transducers. In addition to the responses at 1 and 3, which are the equivalent of those predicted for the Figure 9(a) structure, there are major peaks at 2, 4, and 5. Peaks 4 and 5, which were anticipated, are the slow Rayleigh mode of the plate and the slowest bulk shear wave of the crystal. The response at 2 is not predicted by analysis of the Figure 9(a) structure or consideration of other plate or bulk wave modes. However, finite element analysis of the Figure 9(b) waveguide shows that a new mode at V = 2819.1 m/s is introduced by truncating the bottom surface as illustrated. The theoretical values for the modes of Figure 9(b) are shown in Figure 10 and listed in its caption.

The response spur shown at position 2 in Figure 10 is only about -15 dB below the fundamental waveguide mode. Worse still is the fact that its
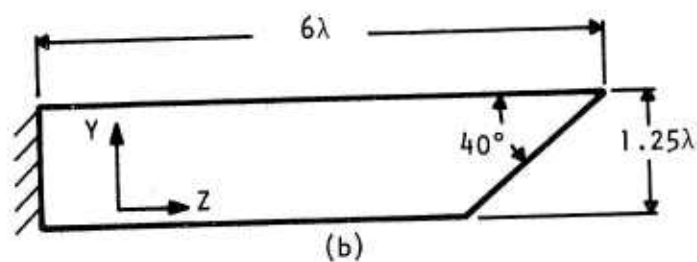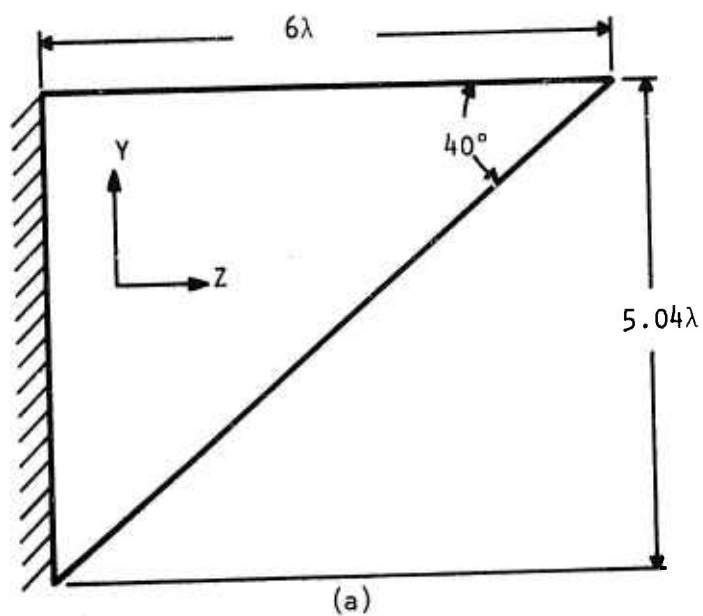
Figure 9 Cross Sections of LiNbO$_3$ Waveguides

(a) Approximation to a waveguide with infinitely large lateral surfaces.

(b) Model of waveguide actually built.
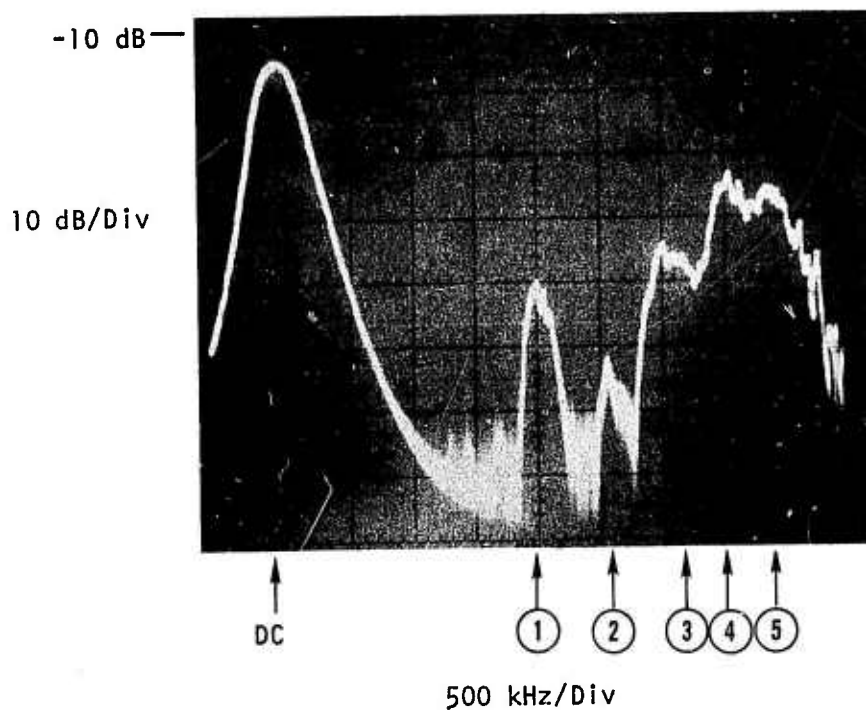
Figure 10 Frequency Response Characteristics for a LiNbO$_3$ Waveguide as Illustrated in Figure 9(b).

1. V = 2160.3 m/sec   Fundamental antisymmetric flexural mode
2. V = 2819.1 m/sec   First higher order waveguide mode
3. V = 3410.7 m/sec   Second higher order waveguide mode
4. V = 3708.1 m/sec   Rayleigh mode of plate
5. V = 4078.0 m/sec   Bulk shear wave

frequency is close enough to the fundamental that matching networks cannot effectively discriminate against it. Figure 11 shows the waveguide frequency response after LC matching at the fundamental mode. The spurious responses at 2 and 3 are now down about 20 dB from the main response, while the responses at 4 and 5 have been rolled off significantly by the matching network.

It is of interest to note that at midband of the fundamental mode, the minimum insertion loss to a peak of the triple transit ripple is only 6 dB. An average through the midband response indicates that without triple transit ripple the insertion loss would be on the order of 9 dB.

D. Experimental Evaluation of Transducer Apodization

1. Substrate Orientation

To evaluate the effects of apodization on transducer coupling, a substrate orientation was sought that would provide as much strong coupling, over as large a region, as possible. In search of such a cut, we examined all the principal directions of propagation in LiNbO$_3$ with top surfaces cut perpendicular to a major axis and the top angle at 40°. The qualities sought were large $\Delta V/V$ and an electric potential that was real, that did not change sign along the top surface of the waveguide, and that decayed away from the apex as slowly as possible.

Table I shows the theoretical results obtained for the various axis combinations. Note that only four of the possibilities have an electric potential that does not change sign. Of these, the Z-cut, Y-point (or -Z-cut, -Y-point) option provides both the most slowly varying electric potential and the strongest coupling ($\Delta V/V$).

Plots of the electric potential and the particle displacements of the lowest-order waveguide mode for the Z-cut, Y-point LiNbO$_3$ waveguide are given

20

0 dB

10 dB/Div

500 kHz/Div

0 dB
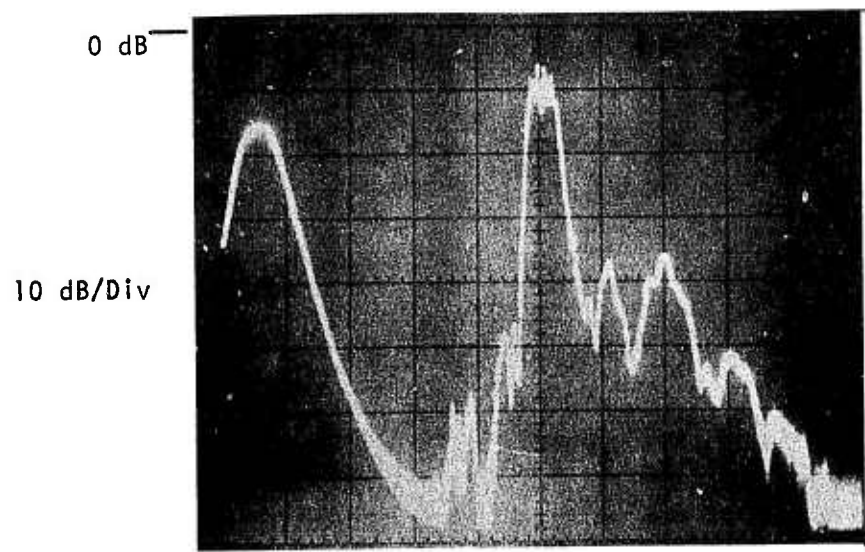
10 dB/Div
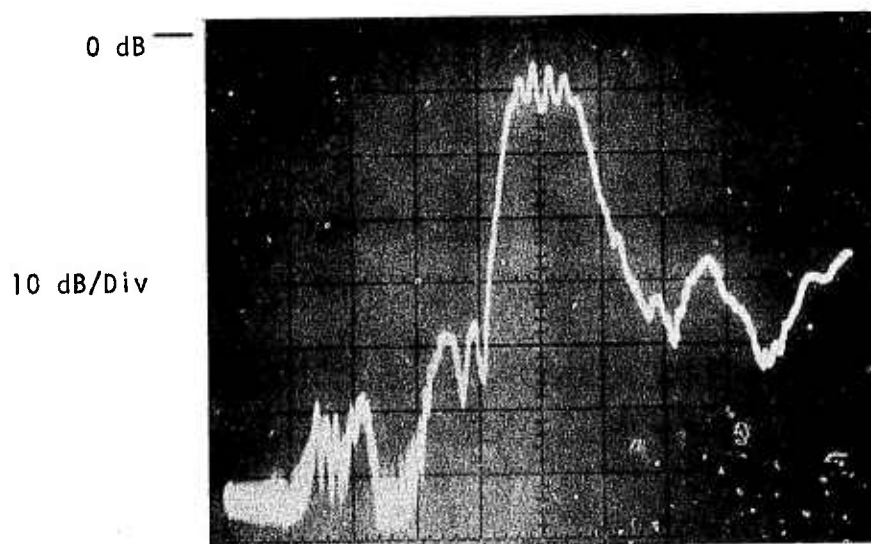
200 kHz/Div

Figure 11   Frequency Response of the LiNbO$_3$ Delay Line of
Figure 9(b) after Matching the Transducers to a
50 Ω System.   Center frequency is 2.24 MHz.

21

Table I
Characteristics of 40° Top Angle LiNbO$_3$ Waveguides

Top	Point	ΔV/V	Electric Potential			Velocity
			Real	Complex	Sign Change	
X	Y	0.00732		yes	yes	2310.87
X	-Y	0.00734		yes	yes	2310.85
X	Z	0.00622		yes	yes	2334.27
X	-Z	0.00622		yes	yes	2334.17
-X	Y	0.00734		yes	yes	2310.85
-X	-Y	0.00731		yes	yes	2310.87
-X	Z	0.00622		yes	yes	2334.17
-X	-Z	0.00622		yes	yes	2334.27
Y	Z	0.0224	yes		(no)	2340.41
Y	-Z	0.00367	yes		yes	2274.22
Y	X	0.00573		yes	yes	2315.36
Y	-X	0.00573		yes	yes	2315.36
-Y	Z	0.00367	yes		yes	2274.22
-Y	-Z	0.0224	yes		(no)	2340.41
-Y	X	0.00573		yes	yes	2315.36
-Y	-X	0.00573		yes	yes	2315.36
Z	X	0.0251		yes	yes	2462.40
Z	-X	0.0251		yes	yes	2462.37
Z	Y	0.0294	yes		(no)	2441.78
Z	-Y	0.0155	yes		yes	2409.16
-Z	X	0.0251		yes	yes	2462.37
-Z	-X	0.0251		yes	yes	2462.40
-Z	Y	0.0155	yes		yes	2409.16
-Z	-Y	0.0294	yes		(no)	2441.72

Note: Top refers to the crystal axis normal to the upper surface of the wave-
guide. Point refers to the crystal axis in the plane of the upper surface and
pointing toward the waveguide apex. ΔV/V gives the variation in velocity due
to shorting the top surface. The columns Real, Complex, and Sign Change tell
whether the electric potential is real or complex and whether it goes through
zero anywhere along the top surface of the waveguide. The velocity shown and
electric potential data refer to the lowest order antisymmetric flexural mode
of the waveguide.

in Figure 12. Throughout the first 3 λ from the apex the electric potential is large. This is in contrast to the behavior of the particle displacements, which decay to a small value by 3 λ from the apex.

Because of the electrical properties of the Z-cut, Y-point waveguide orientation, it was chosen for the tests of apodized transducers. The waveguides, which were mechanically polished, had a top surface dimension of 0.240 inch (6 λ) and a 40° top angle. A free propagation distance of 0.290 inch (7.25 λ) was allowed between the N = 10.5 transducers. The electrodes were 3 λ long. With a wavelength of 0.040 inch the center frequency was approximately 2.3 MHz. An illustration of the LiNbO$_3$ waveguide configuration considered is shown in Figure 13 along with a photograph of one of the devices tested.

Figure 14 shows the transmission characteristics for four values of apodization. With the full overlap transducers (3 λ) the delay line had an insertion loss of 49 dB; the 2.75 λ overlap transducers gave 51 dB; and the 2.5 λ and 2.25 λ overlap transducers produced 54 dB and 58 dB, respectively. The effects of apodization on the insertion losses are clear and much stronger than we had anticipated. The signal falls off so rapidly with increasing apodization that by an overlap of 2.0 λ the waveguide mode was down in the crosstalk level.

2. Radiation Resistance Measurement

While the insertion loss results of Figure 14 show the strong effect of apodization, they do not provide a direct measure of radiation conductance. Other factors enter into the overall insertion loss result to obscure the exact effect of apodization on radiation conductance. For example, variations in the impedance mismatch occur, propagation losses vary with the defects in the waveguide apex, and dispersion variations may lead to different center frequencies for the two transducers of the delay line. As a consequence of

23
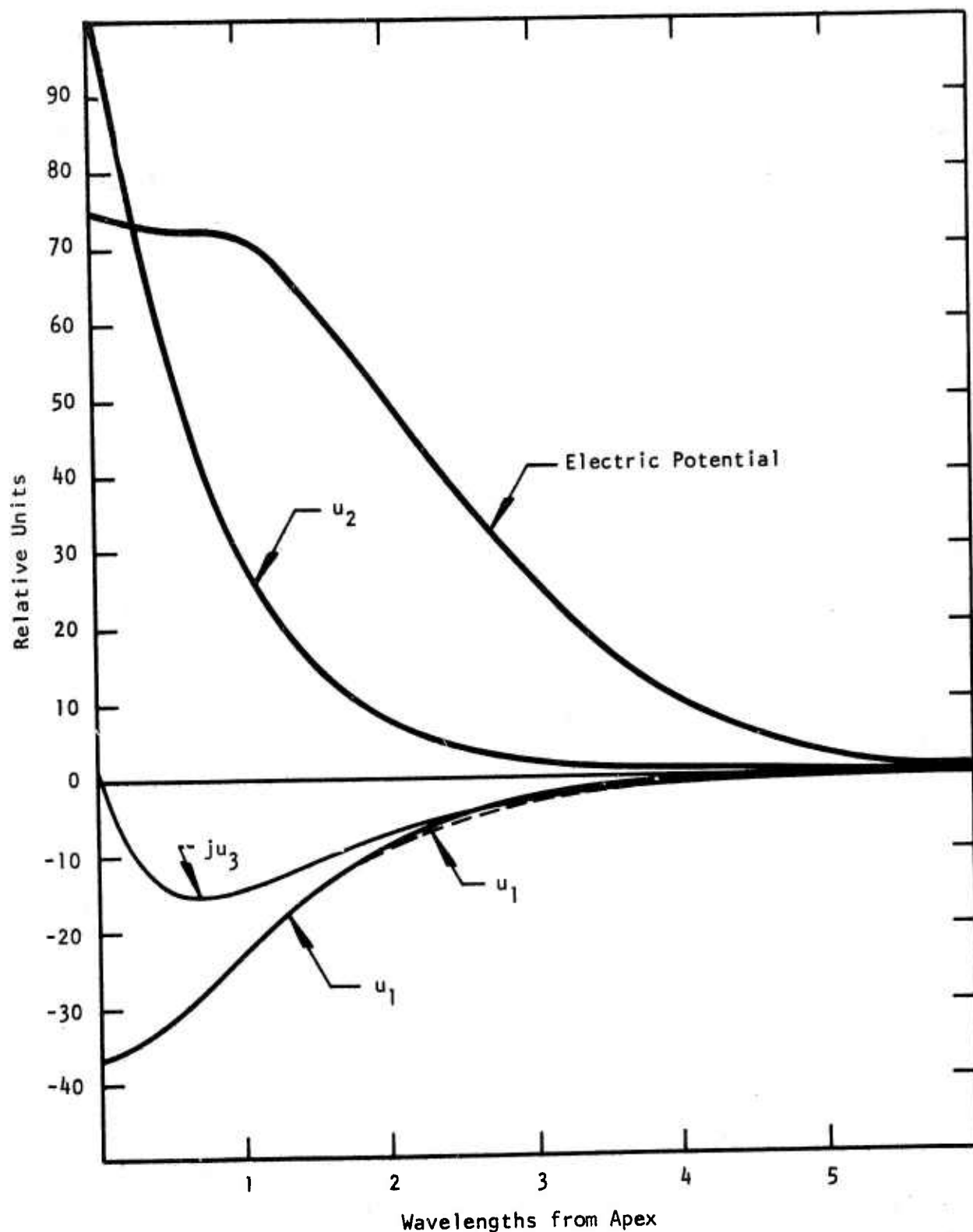
Figure 12 Field Quantities for the Lowest Order Mode of a Z-Cut, Y-Point $LiNbO_3$ Waveguide. The dashed curve shows the variation in the u_1 particle displacement when the top surface of the waveguide is short circuited. Perturbations in the other particle displacements due to electrical shorting of the top surface are less than the linewidths of the curves.

24

(a)

(b)
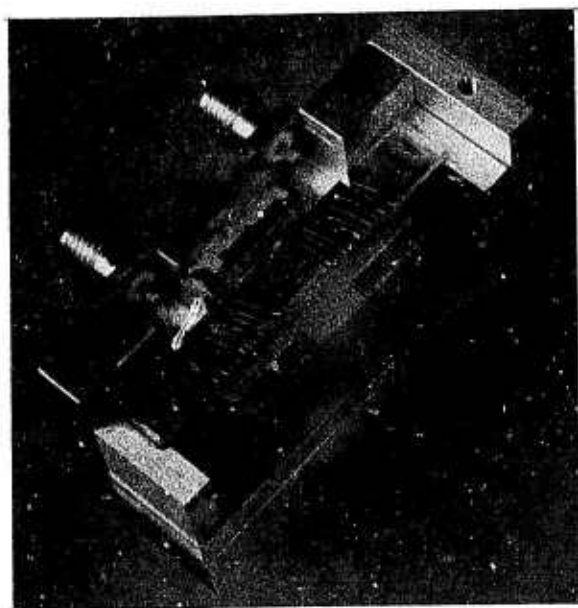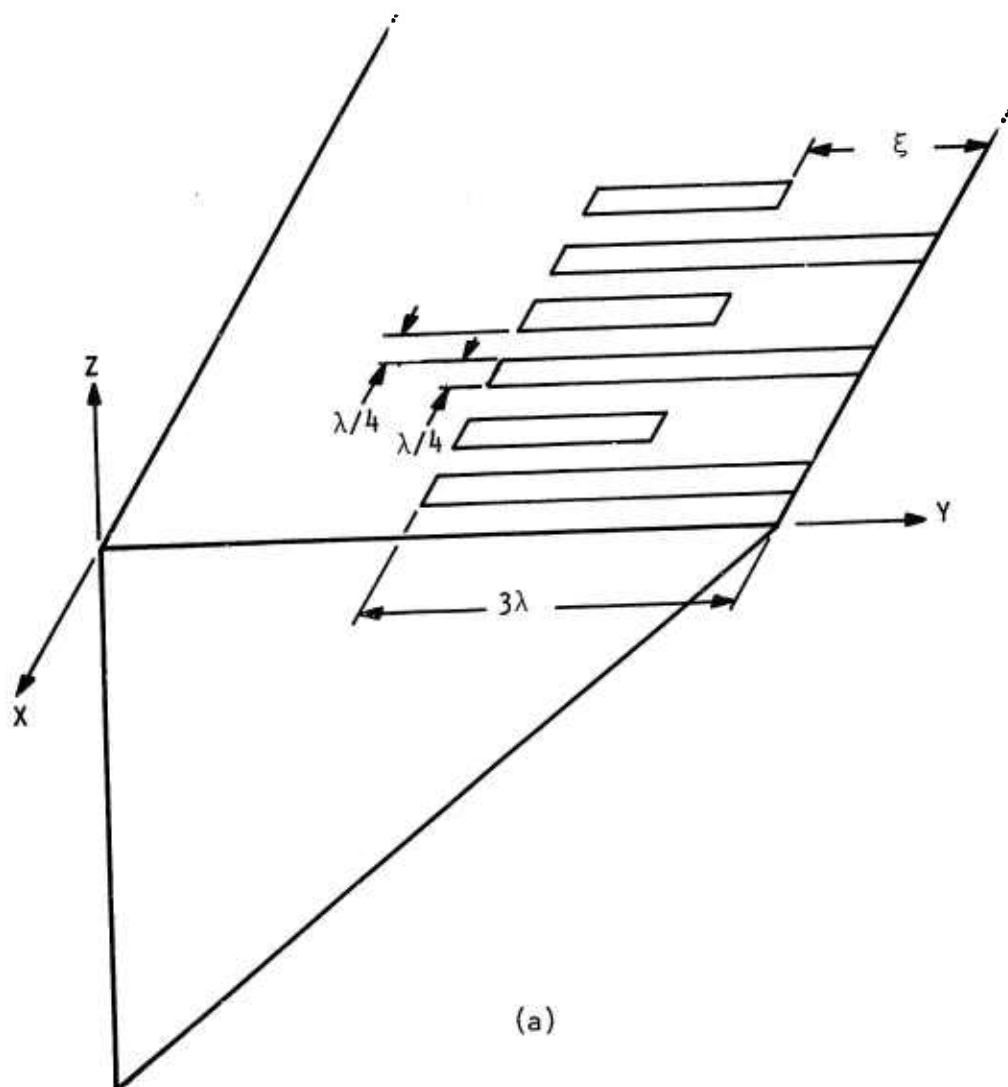
Figure 13 (a) Illustration of Apodized ID Transducers Evaluated. (b) Photograph of LiNbO$_3$ Waveguide Delay Line in Test Fixture.
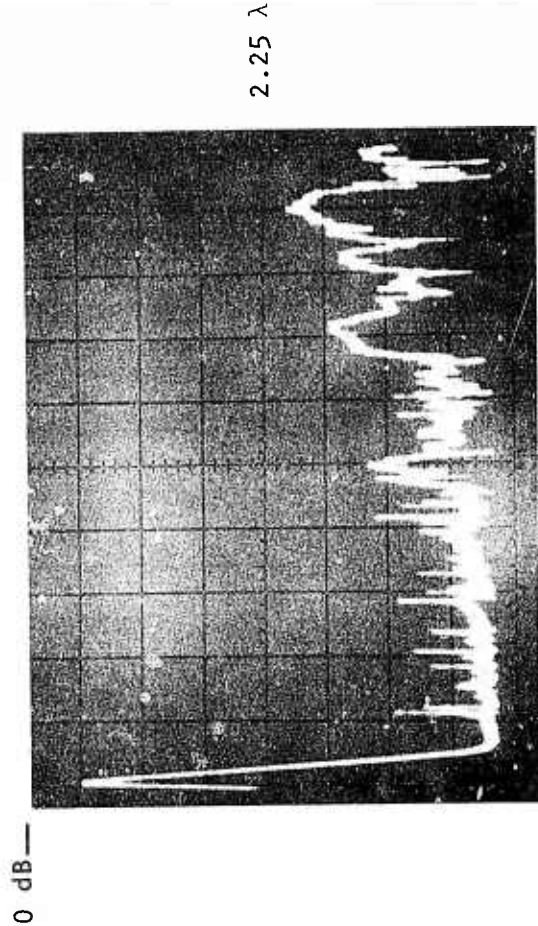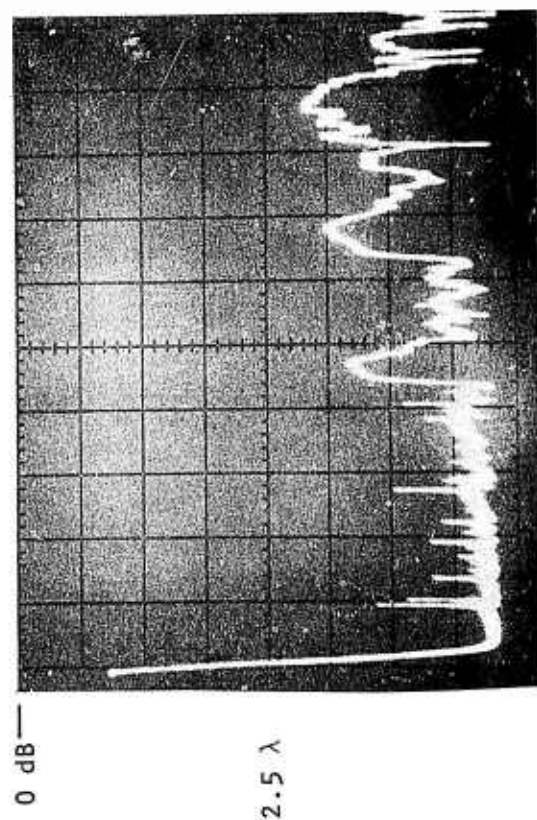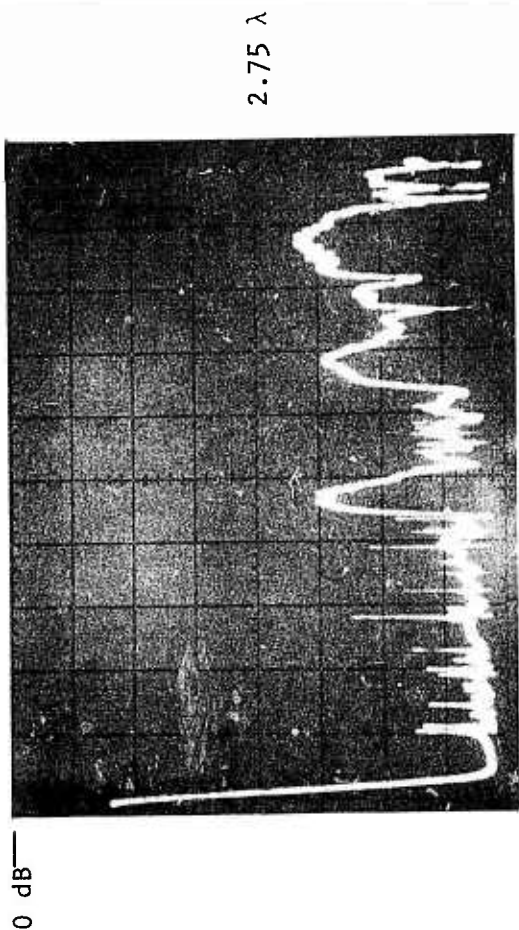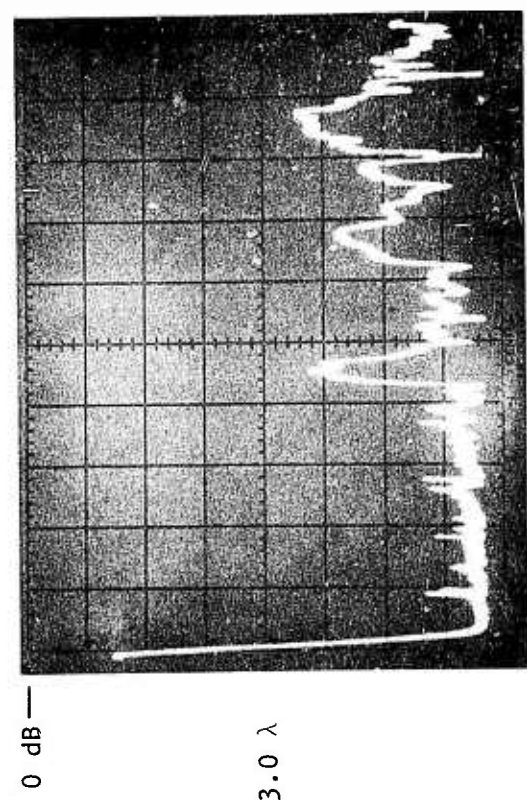
Figure 14 Frequency Responses of Z-Cut, Y-Point LiNbO₃ Waveguide Delay Lines with Apodized Transducers. Interdigital electrode overlaps of 3.0 λ, 2.75 λ, 2.5 λ, and 2.25 λ were considered. In all cases, ordinate is 10 dB/Div and abscissa is 0.5 MHz/Div.

26

these possibilities we measured the radiation resistance of the waveguides directly.

We found series equivalent circuits for the transducer impedances. Typically, the impedance was on the order of (600 -j6000) Ω at 2.3 MHz. Attempts to measure the real part of impedances of this order accurately using standard instrumentation met with poor success. Instead, we built the bridge arrangement described below.

Figure 15 shows the circuit used to measure the waveguide transducer impedances. Basically it is a standard bridge arrangement with R_a and C_t representing the waveguide transducer. The two 10 pF fixed capacitors were hand-picked to be identical at 2.3 MHz. More important, though, are the stray capacitances shown at A and B. The stray capacitance at A was set by the connector to the transducer, by standoff capacitance, and by connector provision for the introduction of a vector voltmeter at that point. The stray capacitance at B was adjusted to balance that at A by introducing identical standoffs and connectors. We found that the magnitudes of the stray capacitances were not important so long as they were balanced.

Even though the 0 to 2 kΩ Techno resistor was wire-wound, its parallel equivalent circuit at 2.3 MHz was very nearly that of the resistor alone. It looked like a resistor in parallel with ± 3 pF maximum over the 20 Ω to 2 kΩ range of the resistor. Thus, at the largest value of resistance encountered in the measurement, 1100 Ω, and at the worst case for shunt capacitance, 3 pF, the potentiometer looked like 1.1 kΩ in parallel with -j23 kΩ. The value of resistance at 2.3 MHz was always within 20 Ω of the value measured at dc across the terminals of the potentiometer. A calibration check where we used known resistors in place of the waveguide transducer produced the following results:
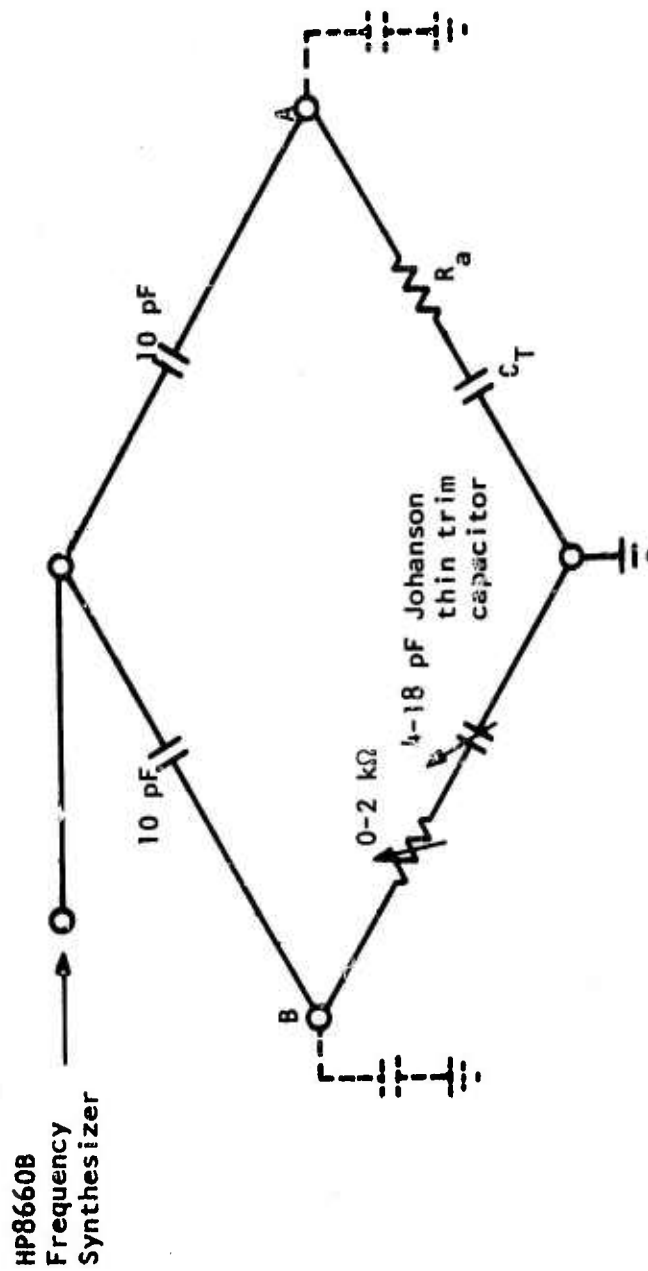
Figure 15 Bridge Circuit for Measuring the Radiation Conductance of the Apodized Transducers. R_a and C_T represent the transducer of the waveguide.

Measured	Known
67 Ω	80 Ω
150 Ω	170 Ω
190 Ω	195 Ω
386 Ω	410 Ω
796 Ω	838 Ω
1.45 Ω	1.48 Ω

The signal source was an HP8600B frequency synthesizer; voltages were measured with an HP8405A vector voltmeter. Without the stability of a quality signal source like that used, the phase readings of the vector voltmeter were not solid enough to produce accurate measurements. With this equipment we found that repeatability was better than the absolute accuracy of the technique.

The measurements were carried out by (1) reading the amplitude and setting the phase reference of the voltage at A with the vector voltmeter; (2) monitoring the voltage at B while adjusting the thin trim capacitor to obtain the source voltage magnitude; and (3) with the voltmeter still at B, adjusting the potentiometer to produce the same phase as at A. Sometimes this procedure might require a second iteration for accurate balance, but for small frequency increments the magnitude and phase adjustments were sufficiently orthogonal so that changing the value of R in step 3 did not react on the magnitude adjustment in step 2.

Measured radiation resistances for four apodizations are shown in Figure 16. The largest midband value obtained was ∿ 1100 Ω, while the smallest was on the order of 300 Ω. This rate of decrease in the radiation conductance is much faster than the electric potential fall-off. Also, we found that spurious acoustic activity was enhanced as the transducer was apodized. Indications of increased spurious effects are seen in the peaks showing up in the radiation resistance of the 2.25 λ overlap device. We believe that these peaks

29
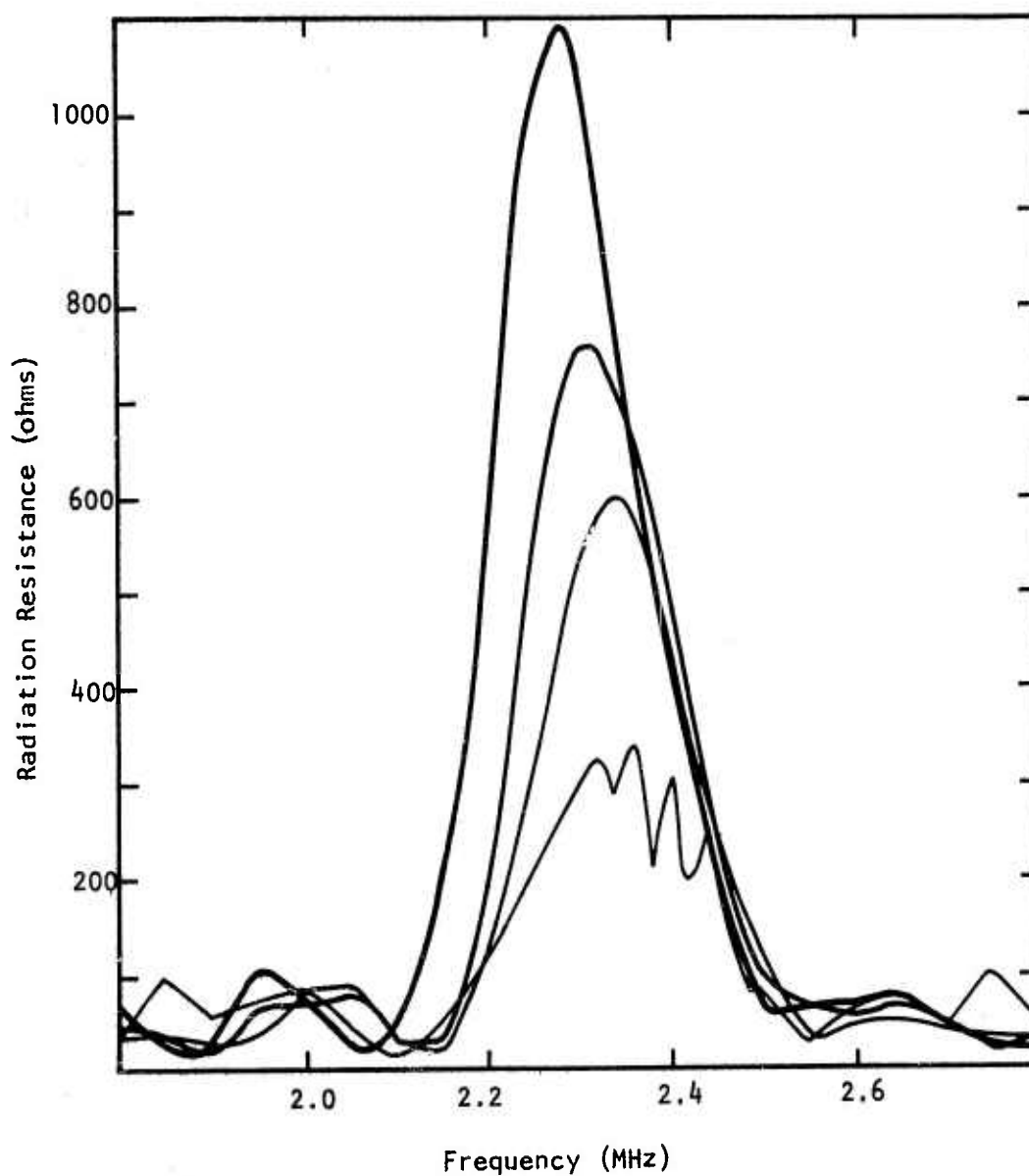
Figure 16   Radiation Resistances of the Apodized Transducers.   Within
the first 0.75 λ of apodization, the midband resistance drops
from ∿ 1100 Ω to ∿ 300 Ω.

represent energy input to modes other than the waveguide mode; however, direct evidence that this is so has not been obtained.

A detailed theoretical development has been carried out in an effort to explain the rapid decrease in transducer coupling evident in Figure 16. The theory presented in the next sections predicts a fairly rapid decrease in G_a, but still not as rapid as that seen experimentally.

E.   Interdigital Transducer Impedance as a Function of Apodization

1.   Capacitance

a.   Statement of Equivalent Isotropic Problems

It is clear just from the appearance of the apodized inter-digital transducer shown in Figures 2(c) and 13 that many of the approximations used for SAW transducers are not valid for the wedge waveguide transducer. The wedge waveguide transducer has only 1 to 3 λ of overlap; consequently, the field pattern surrounding the electrodes is composed entirely of what would be considered second-order fringing fields in SAW transducers.

Direct solution for the charge distribution on the electrodes of a solid section is an exceedingly difficult problem. However, some approxima-tions can be made in order to formulate a similar problem that can be solved directly.

Figure 17(a) shows a cross section of the LiNbO$_3$ waveguide we seek to analyze. Figure 17(b) shows an isotropic solid with representative charge samples along the Y and Z axes. We will show that the Figure 17(b) solid can provide a reasonable approximation to the electrostatic fields of the Figure 17(a) wedge.

31
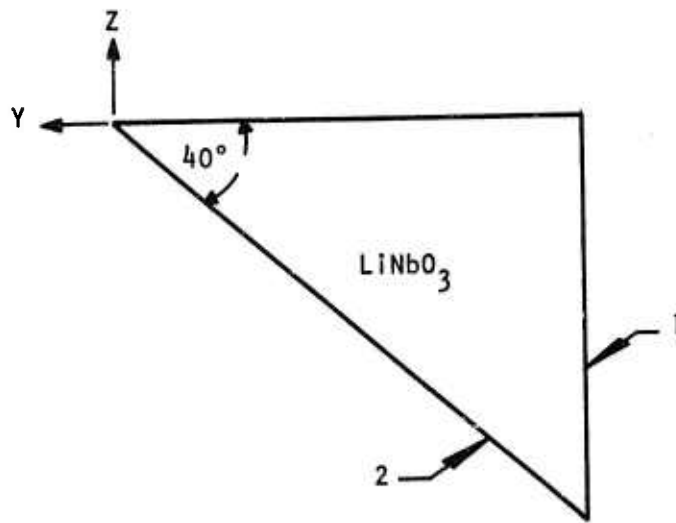
(a)
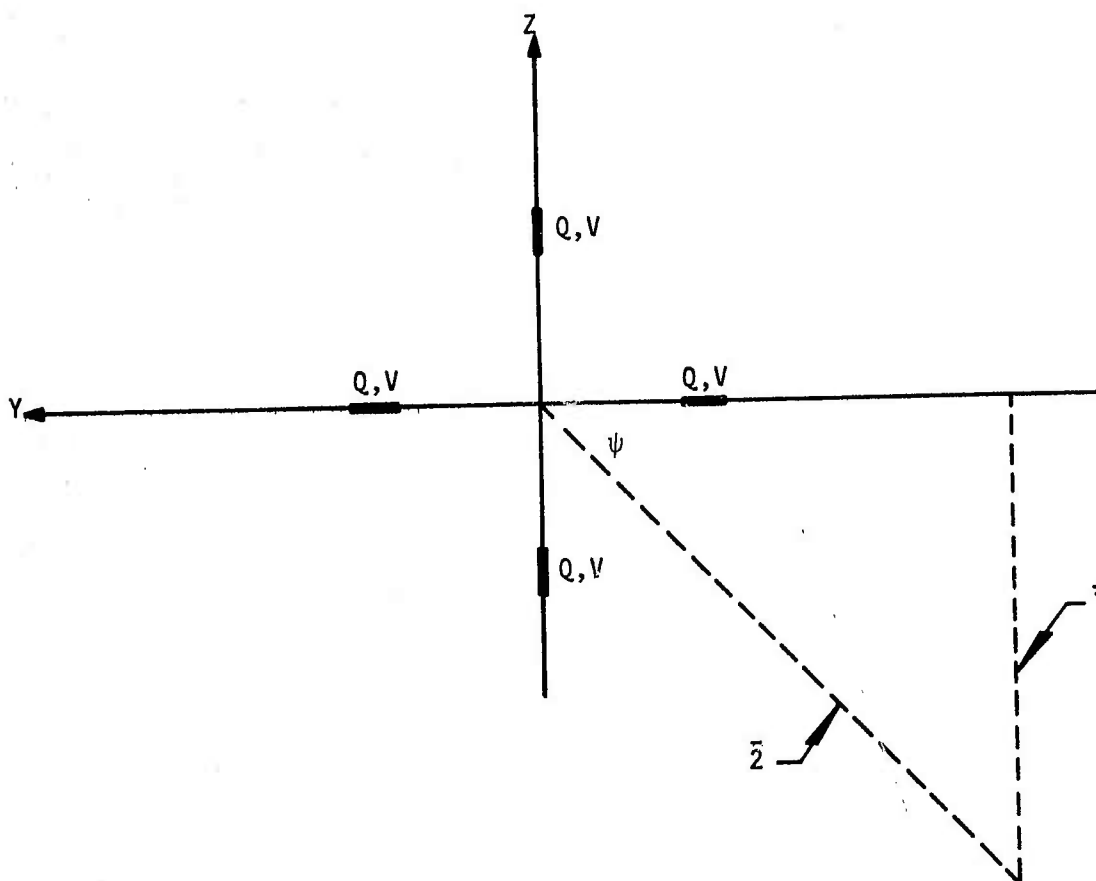
(b)

Figure 17 (a) Z-Cut, Y-Point LiNbO$_3$ Waveguide, (b) Electrostatically
Equivalent Isotropic Solid Space

We will make an approximation that is commonly employed, but that is unquestionably incorrect in the current case. However, the assumption is necessary for the equivalence of the two electrostatic problems. We assume that the dielectric constants of the LiNbO$_3$ are sufficiently large that all fields exterior to the LiNbO$_3$ in Figure 17(a) can be neglected. The mathematical statement of this assumption is that $D_{Normal} = 0$ on all unelectroded surfaces. Then the system of equations describing the field in the wedge is

$$\varepsilon_y \frac{\partial^2 \phi}{\partial x^2} + \varepsilon_y \frac{\partial^2 \phi}{\partial y^2} + \varepsilon_z \frac{\partial^2 \phi}{\partial z^2} = 0 \tag{1}$$

$$\varepsilon_z \frac{\partial \phi}{\partial z} = \rho_z \tag{2}$$

$$D_{Normal} = 0 \tag{3}$$

where Equation (1) is Laplace's equation, and we have made use of the fact that in LiNbO$_3$ $\varepsilon_x = \varepsilon_y$, electrodes only appear on the upper Z surface; Equation (2) is applicable where the surface is electroded; and Equation (3) is applicable on all other surfaces. The electrode and field distribution of the wedge are assumed to be periodic in the X direction.

In order for the fields, and the charge distribution along the negative half of the Y-axis in Figure 17(b), to be equivalent to those in Figure 17(a), it is sufficient (and necessary) that they satisfy the same boundary conditions at the enclosing boundary shown by the dashed lines and the Y-axis in Figure 17(b) as exist at the boundaries of the wedge; it is also necessary that the differential equations for the two problems be the same. We assume that the electrode patterns on the waveguide appear also on the negative Y portion of the Z = 0 plane of the isotropic solid. In addition, we place the pattern in the space three more times by rotating it 90°, 180°, and

270° from its wedge waveguide equivalent position. Samples of the charge on the electrodes are shown in Figure 17(b) labeled Q, V.

By the symmetry of the charges we see that $D_{Normal} = 0$ along the line $\bar{2}$. Also if the charges q extend only a few wavelengths from the X-axis, and the vertical dashed line $\bar{1}$ is taken to be five or more wavelengths from the X-axis, then D tends to zero on that plane also. On the plane Z = 0 we have $D_z = 0$ by symmetry on the unelectroded portion. Thus, we see most of the necessary boundary conditions for equivalence of the two problems are met by symmetry.

The equations governing the electrostatic fields in the isotropic solid are

$$\varepsilon_y \frac{\partial^2 \phi}{\partial x^2} + \varepsilon_y \frac{\partial^2 \phi}{\partial y^2} + \varepsilon_y \frac{\partial^2 \phi}{\partial z^2} = 0 \tag{4}$$

$$-\varepsilon_y \frac{\partial \phi}{\partial z}\bigg|_{z=0^+} + \varepsilon_y \frac{\partial \phi}{\partial z}\bigg|_{z=0^-} = \rho_z \tag{5}$$

$$-\varepsilon_y \frac{\partial \phi}{\partial y}\bigg|_{y=0^+} + \varepsilon_y \frac{\partial \phi}{\partial y}\bigg|_{y=0^-} = \rho_y \quad , \tag{6}$$

where we have labeled the dielectric constant of the isotropic medium ε_y, and Equations (5) and (6) give the discontinuity in electric displacement at charges along the Z = 0 and Y = 0 planes, respectively.

Consider the coordinate change

$$Z = \bar{Z} \sqrt{\frac{\varepsilon_y}{\varepsilon_z}} \quad . \tag{7}$$

34

Then Equation (4) becomes

$$\varepsilon_y \frac{\partial^2 \phi}{\partial x^2} + \varepsilon_y \frac{\partial^2 \phi}{\partial y^2} + \varepsilon_z \frac{\partial^2 \phi}{\partial z^2} = 0 \quad . \tag{8}$$

Thus, Laplace's equation, Equation (8), in the distorted solid becomes the same as that for the LiNbO$_3$ wedge, Equation (1).

Applying the coordinate change to Equation (5) we find

$$-\varepsilon_z \left. \frac{\partial \phi}{\partial z} \right|_{z=0^+} + \varepsilon_z \left. \frac{\partial \phi}{\partial z} \right|_{z=0} = \sqrt{\frac{\varepsilon_z}{\varepsilon_y}} \, \rho_z \quad . \tag{9}$$

By symmetry the electric field above and below z = 0 has the same magnitude. Thus, we can write

$$\varepsilon_z \left. \frac{\partial \phi}{\partial z} \right|_{z=0} = \frac{1}{2} \sqrt{\frac{\varepsilon_z}{\varepsilon_y}} \, \rho_z \quad . \tag{10}$$

Equation (1) has the same form as Equation (2). We see, therefore, that in the isotropic problem of Figure 12(b), if the coordinate transformation of Equation (7) is applied, then the governing equations for the two problems become the same. The boundary conditions for the two problems become nearly the same, i.e.:

(1) The boundary condition of $D_y = 0$ on surface $\bar{1}$ is satisfied.

(2) The boundary condition of $D_z = 0$ on z = 0 where there are no electrodes is satisfied by symmetry.

(3) Equation (2) gives the boundary condition on D_z at z = 0 for the LiNbO$_3$ wedge. Equation (10) gives the boundary condition on D_z at z = 0 in the modified isotropic space. The charge density of the wedge transducer ρ_z^w is obtained from the charge density of the isotropic space by

35

$$\rho_z^w = \frac{1}{2} \sqrt{\frac{\epsilon_z}{\epsilon_y}} \, \rho_z^I \quad . \tag{11}$$

(4) In the isotropic problem before coordinate transformation surface $\bar{2}$, on which D_{Normal} vanished, was at $45°$. For the modified problem the $45°$ line moves to

$$\psi = \tan^{-1}[\sqrt{\frac{\epsilon_z}{\epsilon_y}}] \cong 30.9° \quad . \tag{12}$$

Thus, we see that the modified isotropic space problem produces answers to the problem of a LiNbO$_3$ wedge with a $30.9°$ top angle instead of a $40°$ top angle. The differences between the solution of a problem valid for a $30.9°$ wedge and the field distribution of a $40°$ wedge would be most significant at the apex where surface 2 is closest to the charge on the $z = 0$ surface. At distances further from the apex on the $z = 0$ plane where surface 2 at position y is many wavelengths from the charge at position y it is expected that the charge at y would feel the influence of the bottom surface of the wedge only through the charge distribution at positions closer to the apex. Thus, we expect the solutions to be incorrect only near the apex of the wedge.

However, the effect of a $30.9°$ instead of $40°$ apex angle on the charge density near the apex is small in comparison to the effect of assuming that D_{Normal} vanishes on all unelectroded surfaces. Because D_{Normal} was required to vanish on surfaces 2 and $\bar{2}$, the charge density at the apex will go to zero independent of the acute apex angle chosen. This, we believe, is not physically correct. It constitutes the most significant departure from the actual fields caused by making approximations to render the problem analytically tractable.

b. Variational Formulation Problem

Even the equivalent isotropic problem shown schematically in Figure 17(b) is a difficult one to solve exactly. Instead, we have chosen to

approximate the field pattern by minimizing a functional which is stationary with respect to variations about the exact field pattern. The functional,

$$F = \int_0^\lambda \int_{-L}^{L} \int_{-L}^{L} dxdydz \ [(\frac{\partial \phi}{\partial x})^2 + (\frac{\partial \phi}{\partial y})^2 + (\frac{\partial \phi}{\partial z})^2] - \frac{2}{\varepsilon_y} \int\!\!\int_{electrodes} (\phi - V_0) \ \rho ds \ ,$$

(13)

is designed to be applicable to a solid three-dimensional space with permittivity ε_y; electrode patterns on the $y = 0$ and $z = 0$ interfaces as described in the previous section; periodicity in the x direction of λ; and voltages on the electrodes of $\pm V_0$, which is written symbolically as simple V_0 in the above surface integral. The value of L is chosen large enough that fields from the electrodes have decayed to a small value at $z = \pm L$ and $y = \pm L$. In the cases we computed the electrodes were confined to a region within 3 λ of the x axis, and L was chosen to be 5 λ.

A schematic representation of one period of sample charges on the $Z = 0$ plane is shown in Figure 18. An identical distribution exists on the $Y = 0$ plane also, but is not shown. The analysis proceeds by describing the charge samples shown, finding their associated electric potential, taking a sum of all the charge samples necessary to approximate the full electrode complement, substituting the total representation for the fields into Equation (13), taking variations with respect to the basic amplitudes, and solving for their values. This procedure, which is straightforward in principle, is exceedingly tedious. Consequently, only the briefest sketch of the development will be repeated here.

To represent the charges shown in Figure 18 we assume that the space is periodic along Y and Z as well as X. Periodicity along Y and Z is 2L. Those electrodes at $X = n\lambda$, $-\infty < n < \infty$ are at $+V_0$. The electrodes are each of width $\lambda/4$ (along X). An electrode is made up of many segments at constant X, such as are shown in Figure 18.
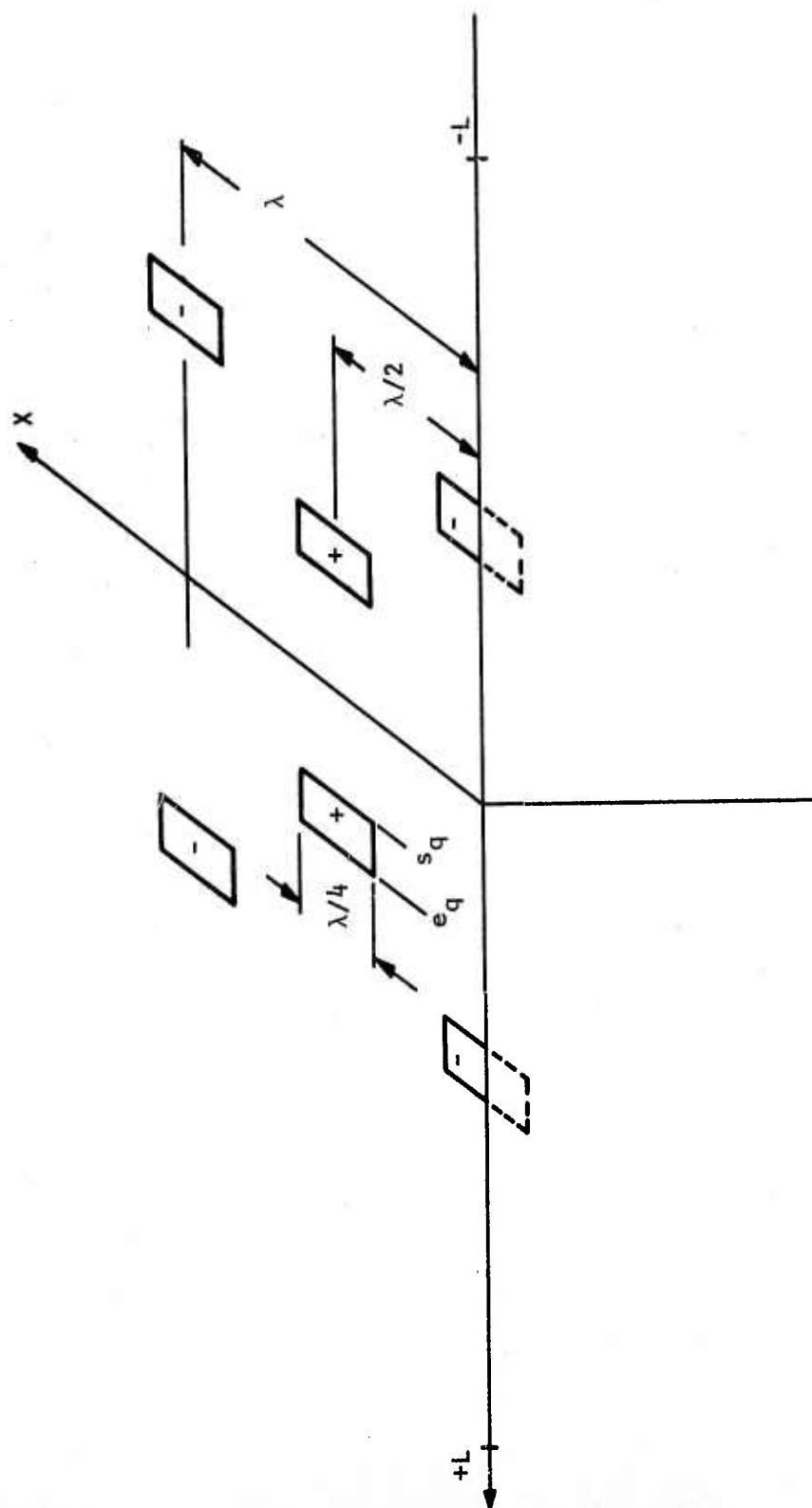
Figure 18 Sample Charges from the Interdigital Electrodes. The remainder of the charges are not shown. Each sample is at a voltage magnitude of $|V_0|$ with a polarity as indicated in the figure.

38

We let q index the charge sample and point to the sample coordinates. Thus, s_q is the starting coordinate of a charge sample and e_q is the ending coordinate. We can then write the total charge density of the entire electrode as a sum over the charge segments indexed by q.

Thus,

$$\rho(x, y, z) = \sum_{q=1}^{N} r_q [R_q(x, y) + R_q(x, z)] \quad , \tag{14}$$

where r_q is the charge density of the qth sample, and R_q is a two-dimensional unit height rectangle function on either the X-Y or X-Z plane. The rectangle functions, of course, represent charge samples of zero thickness and have dimensions $\lambda/4$ along X and $(e_q - s_q)$ along y or z. Direct substitution of the Fourier representations for the charge density into the driving term in Poisson's equation, solution of the equation, and satisfaction of the boundary conditions, give the electric potential:

$$\phi(x, y, z) = \sum_{q=1}^{N} r_q [S_q(x, y, z) + S_q(x, z, y)] \quad , \tag{15}$$

where

$$S_q(x, y, z) = \sum_{n=0}^{\infty} \sum_{m=0}^{\infty} \frac{\delta_n^q A_{nm}^q}{2\varepsilon_y \Gamma_{nm}} \cos\left(n2\pi \frac{x}{\lambda}\right) \cos\left(m\pi \frac{y}{L}\right) e^{\Gamma_{nm} z} \quad , \tag{16}$$

$$\delta_n^q = \begin{cases} 1 & \text{if q points to a negative sample} \\ (-1)^n & \text{if q points to a positive sample} \end{cases} , \tag{17}$$

$$\Gamma_{nm} = \sqrt{\left(\frac{n2\pi}{\lambda}\right)^2 + \left(\frac{m\pi}{L}\right)^2} \quad , \tag{18}$$

$$A^q_{nm} = a_n b_{qm} \quad , \tag{19}$$

$$a_n = \begin{cases} 1/4 & n = 0 \\ \dfrac{2}{n\pi} \sin\left(\dfrac{n\pi}{4}\right) & n \neq 0 \quad , \end{cases} \tag{20}$$

$$b_{qm} = \begin{cases} (e_q - s_q)/L & m = 0 \\ \dfrac{2}{m\pi}\left[\sin\left(m\pi \dfrac{e_q}{L}\right) - \sin\left(m\pi \dfrac{s_q}{L}\right)\right] & m \neq 0 \quad , \end{cases} \tag{21}$$

and

$$R_q(x, y) = \sum_{n=0}^{\infty} \sum_{m=0}^{\infty} \delta^q_n A^q_{nm} \cos\left(n2\pi \frac{x}{\lambda}\right) \cos\left(m\pi \frac{y}{L}\right) \quad . \tag{22}$$

We see from the above results that Equations (14), (22), (17), (19), (20), and (21) give explicit analytic representations for a charge sample on an electrode when values for e_q, s_q, and L are provided. The amplitudes of the charge samples r_q are the only unknown quantities. In addition, Equations (15) and (16) give the self-consistent electric potential associated with the qth charge sample in terms of known parameters and the unknown amplitudes, r_q.

To complete the description of the electrostatic fields we need only find all the r_q representing one period of the transducer. These are found by substituting the expressions for charge density and electric potential from Equations (14) and (15) into the functional, Equation (13), and taking variations. Carrying out the differentiation and volume integral, the problem reduces to the following form:

$$\sum_{q=1}^{n} \left(\frac{\bar{L}}{\pi}\right)^2 \{ \sum_{n=0}^{\infty} \sum_{m=0}^{\infty} \delta_n^h \delta_n^q \Delta_n a_n^2 b_{hm} [\frac{\Delta_m \pi}{\bar{L}} \frac{B_{qm}}{\sqrt{(2n)^2 + (\frac{m}{\bar{L}})^2}}$$

$$+ \sum_{n=0}^{\infty} \frac{b_{qk}}{\bar{L}^2[(2n)^2 + (\frac{m}{\bar{L}})^2] + k^2}]\} \bar{r}_q = P_h \frac{[e_h - s_h]}{\lambda} \quad , \tag{23}$$

where

$$\Delta_n = \begin{cases} 1 & n = 0 \\ 1/2 & n \neq 0 \end{cases} ,$$

$$\bar{r}_q = \frac{2\lambda}{\varepsilon_y |V_0|} r_q \quad , \tag{24}$$

$\bar{L} = L/\lambda$, and P_h is the polarity of the voltage on the hth charge sample. The index h runs from 1 to n, just as q does.

      In most of the numerical work the matrices were approximately of order 20. We could work with such small matrices because of the small electrode sizes. We considered apodized transducers like that shown in Figure 19 with typical electrode sampling as indicated. Illustrated are 3 λ long major electrodes and 2.5 λ long opposing electrodes on a 5 λ wedge. All electrodes are $\lambda/4$ wide. Eleven samples were used on the 3 λ electrodes, and 9 samples on the 2.5 λ electrodes to approximate the charge density.

      The peaks in charge density at the ends of the electrodes are what would naturally be expected; consequently, the indicated behavior of the charge density at the apex is believed to be an unrealistic approximation to the actual charge. Whatever the correct charge density, the results obtained from this analysis would always show $\rho = 0$ at the apex, since we assume D_{Normal} vanished on the bottom surface of the waveguide.
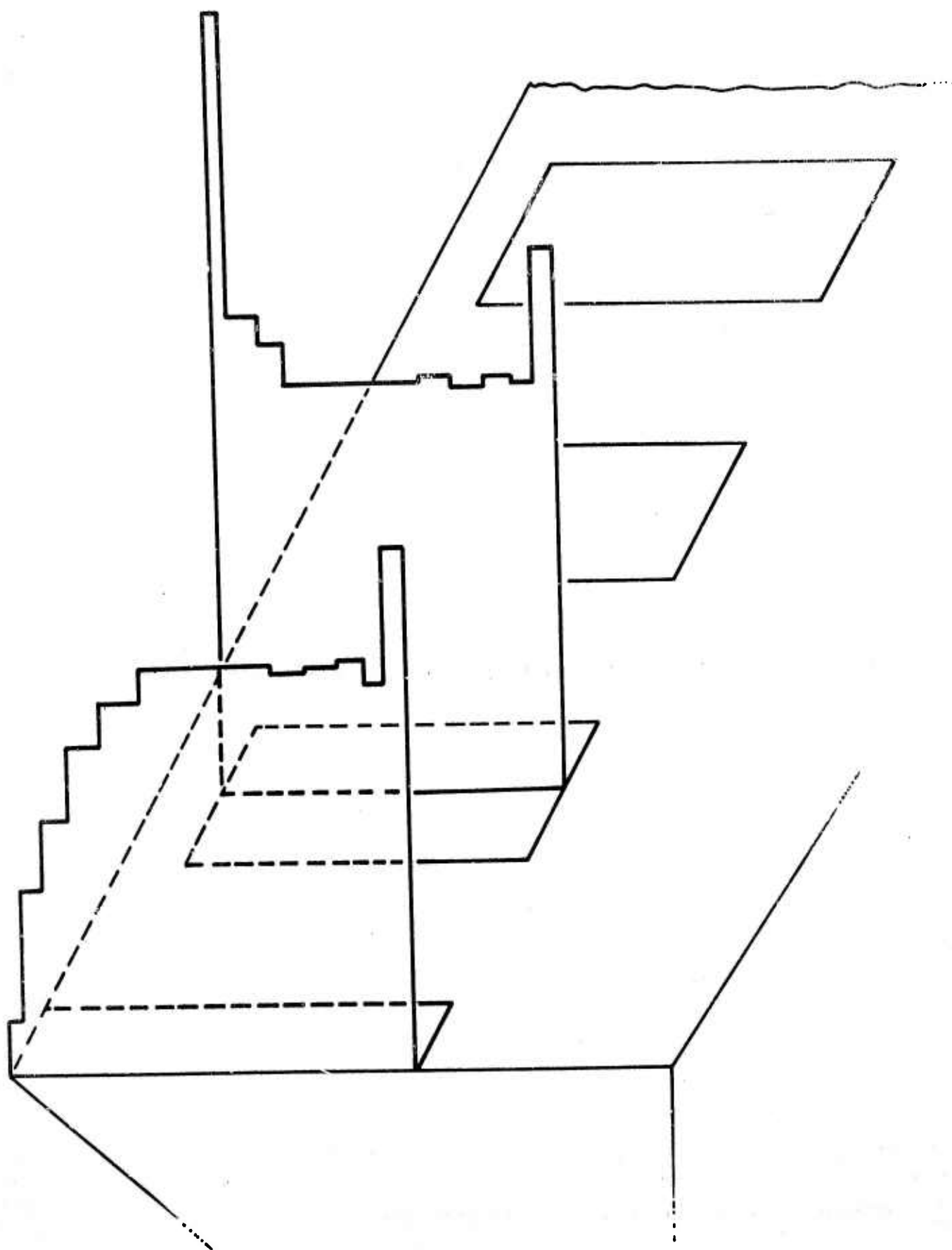
Figure 19   Charge Density Variation Along the Electrodes in an Apodized
Transducer.   In the case illustrated, the electrodes alternate
between 3.0 λ and 2.5 λ.

To facilitate comparison of the charge densities found for various apodizations, a smooth curve was drawn through the pulse samples obtained from the analysis. Charge densities for overlaps of 1.5 λ, 2.0 λ, 2.5 λ, and 3.0 λ are shown in Figure 20. The lower series of curves shows how the charge tends to accumulate in the overlap regions. This is especially pronounced in the 1.5 λ overlap plot where the density from the apex to 1.5 λ is markedly less than that in the remaining 1.5 λ of the electrode.

Two interesting features are evident in the upper set of curves. First the "end effects" are well confined to the ends of the electrodes. With as little as 2.0 λ of overlap, the central region of the electrode begins to display a uniform charge density. The second effect brought out by the curves is the effect of the $D_{Normal} = 0$ condition at the apex. The 2.5 λ overlap curve shows singularities in the charge on both ends. However, when the overlap is increased another 0.5 λ out to the apex of the guide, the pole of charge on the apex end of the electrode turns into a zero.

While the data in Figure 20 may be wrong at the apex of the waveguide, this region is on the order of 0.5 λ long and consequently constitutes a small portion of the total charge distribution. Macroscopic attributes such as transducer capacitance are still adequately described by the sum of the charges found in the analysis. Figure 21 shows capacitance predictions for a 10.5 λ transducer on a Z-cut, Y-point LiNbO$_3$ waveguide. The theoretical curve shows a steady increase in capacitance as the overlap is increased. However, as full overlap is approached, the rate of increase is shown to decline, probably as a result of the $\rho = 0$ problem at the apex as described above. Also shown are experimental results from Z-cut, Y-point LiNbO$_3$ waveguides with 40° top angles. It will be noted that the differences are on the order of 10% throughout. In view of the coarse sampling employed in the analysis, and the $D_{Normal} = 0$ approximation imposed, better agreement could not be expected. Previous analysis[8] has shown that if only one sample

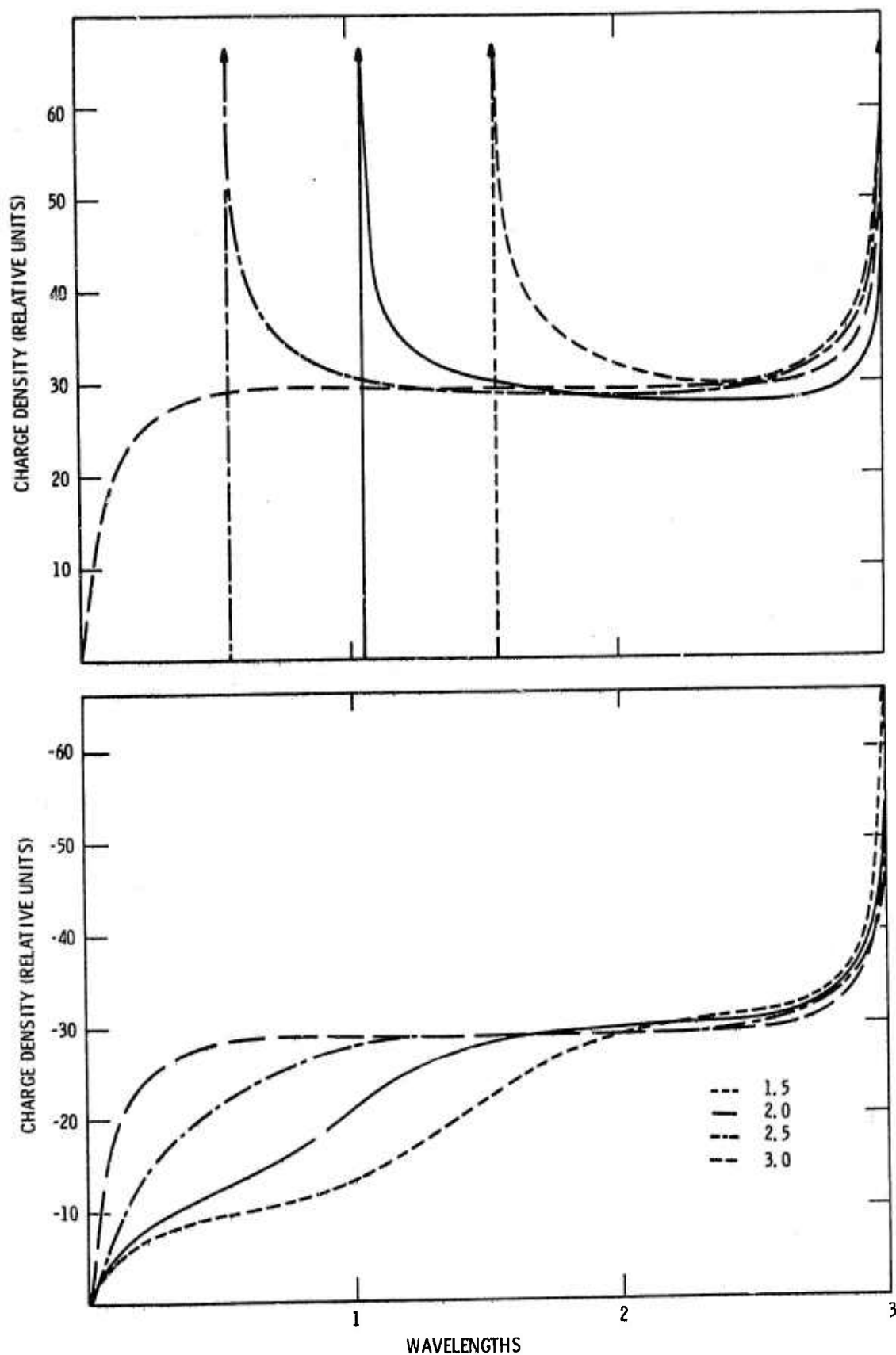Figure 20 "Smoothed" Representations for the Charge Density Variations on Alternate Electrodes of Apodized Transducers with 1.5 λ, 2.0 λ, 2.5 λ, and 3.0 λ of Overlap. Charge densities for shortened electrodes are shown in the upper plots. Results for full-length negative electrodes are given in the lower plots.
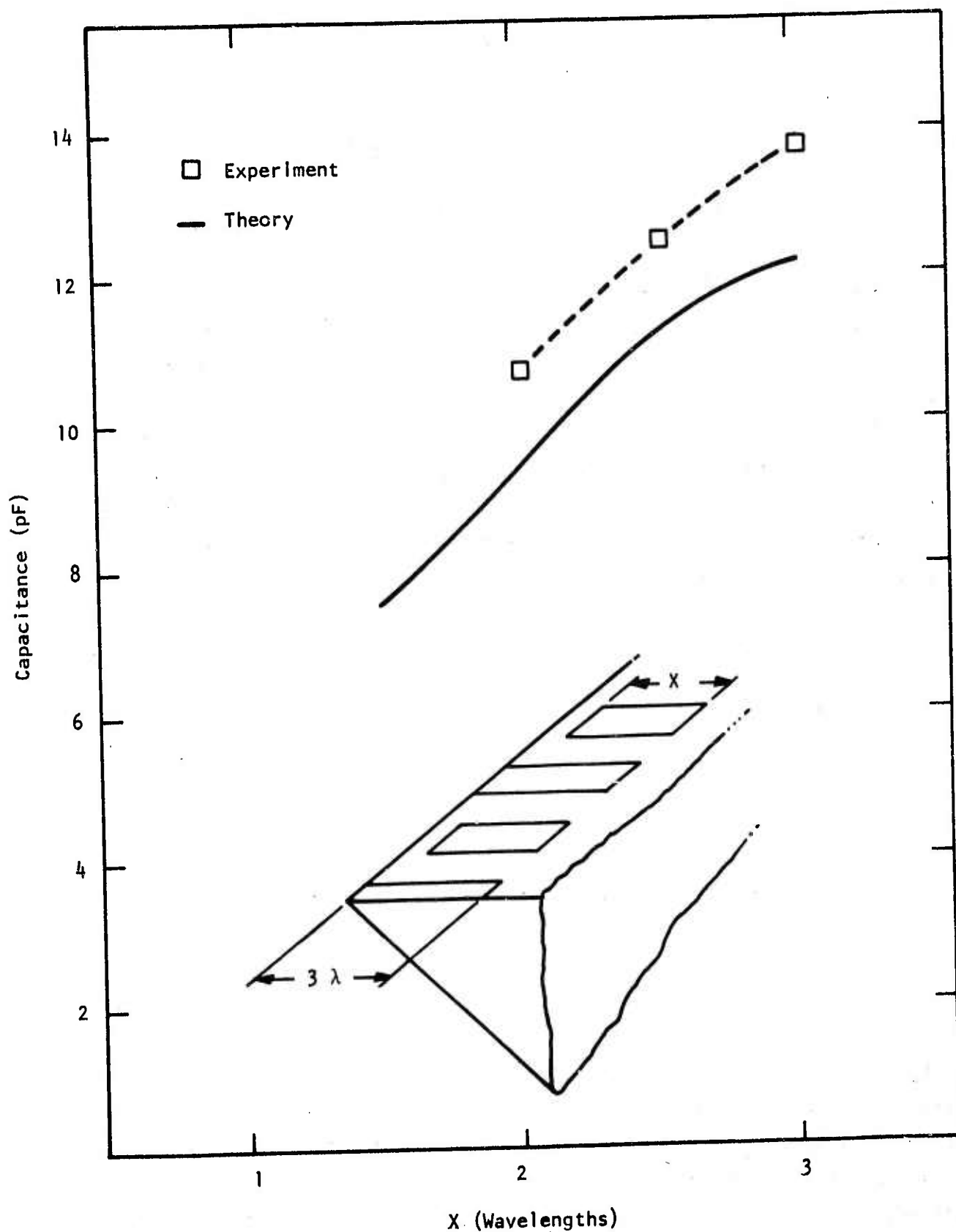
Figure 21 Electrostatic Capacitance Variation as a Function of Overlap for
Apodized Interdigital Transducers

across the width of the electrode is used, the results are ∿ 8% low in value. If we arbitrarily adjusted our prediction upward by 8%, then the differences between experiment and theory would be negligible.

2. Radiation Conductance

The major reason for calculating the charge distribution versus apodization in the previous section was to compute its effect on radiation conductance, not to find the static capacitance. As Figure 21 shows, the variation in capacitance may be 20 to 40%; however, the variation in conductance may be twice that large. Moreover, the capacitance variation influences the energy converted to acoustic waves through the impedance match of the transducer, which is an indirect effect, whereas the value of the conductance influences the energy conversion directly.

The calculation for the radiation conductance of an apodized waveguide transducer is also a rather long exercise. We will thus only sketch the procedure, commenting on the similarity of this development to other published work.

We follow a general approach like that of Auld[9] in his derivation of the radiation conductance for an interdigital SAW transducer. When we allow for variation along the crests of the wave, the result equivalent to his Equation 10.134 is

$$4P_{nn}[\frac{d}{dz} + j\beta_n] \, a_n(z) = \oint [\vec{V}_n^* \cdot \vec{T}_1 + \phi_n^*(j\omega\vec{D}_1)] \cdot d\vec{\ell} \, , \qquad (25)$$

where P_{nn} is the power flow through a cross section of the waveguide, β_n is the propagation constant of a normal mode of the guide, a_n is the amplitude of the normal mode, V_n^* and ϕ_n^* are the complex conjugates of the velocity field and electric potential of the nth mode, $\vec{T}_1$, and $\vec{D}_1$ are the stress and electric displacement fields in the transducer region, and the line integral is taken

46

completely around the waveguide exterior, but under the electrodes. If we neglect the stress under the electrodes and let the nth mode be either the forward or the backward lowest order mode of the waveguide, we obtain differential equations for the excited modes:

forward $\quad [\frac{d}{dz} + j\beta_G] \, a_{G+}(x) = \frac{-1}{4P_G} \oint \phi_{G+}^* (j\omega\vec{D}_1) \cdot d\vec{\ell}$, $\qquad (26)$

backward $\quad [\frac{d}{dz} - j\beta_G] \, a_{G-}(x) = \frac{1}{4P_G} \oint \phi_{G-}^* (j\omega D_1) \cdot d\vec{\ell}$. $\qquad (27)$

In these equations the only functions of x are $a_{G+}(x)$, $a_{G-}(x)$, and $\vec{D}_1$. The electric potential we assumed to vary as $\exp[\pm j\beta_G x]$, and the factor has been divided out.

Since we have assumed that D_{Normal} vanishes everywhere except under an electrode, we need only find a representation for $\vec{D}_1$ in a driven transducer and carry out the integral over the transducer region, which in our case is from the apex to 3 λ.

The $\vec{D}$ field we write in general as

$$D_1 = g(x) \, h(y) \quad , \qquad (28)$$

where g(x) is a pulse train along the x direction, and h(y) is the static charge distribution found in the previous section. In fact, D_1 will be written as a sum of two terms such as in Equation (28), one expression for each polarity of electrodes. After finding Fourier series representations for g(x), Equations (26) and (27) can be reduced to

$$[\frac{d}{dx} + j\beta_G] \, a_{G+}(x) = -[\Gamma_I \, P_1(x) + \Gamma_2 \, P_{II}(x)] \quad , \qquad (29)$$

$$\left[\frac{d}{dx} - j\beta_G\right] a_G(x) = \left[\Gamma_3 P_I(x) + \Gamma_4 P_{II}(x)\right] \quad , \tag{30}$$

where P_I is a pulse train with pulses of width $\lambda/4$ centered on $x = n\lambda$, P_{II} is a pulse train with pulses of width $\lambda/4$ centered on $x = (n + 1/2)\lambda$,

$$\Gamma_1 = \frac{-1}{4P_G} \int_{-3\lambda}^{0} j\omega \phi_{G+}^*(y) \, Q_-(y) \, dy \quad , \tag{31}$$

$$\Gamma_2 = \frac{1}{4P_G} \int_{-3\lambda}^{\xi} j\omega \phi_{G+}^*(y) \, Q_+(y) \, dy \quad , \tag{32}$$

$$\Gamma_3 = -\Gamma_1^* \quad , \tag{33}$$

$$\Gamma_4 = -\Gamma_2^* \quad , \tag{34}$$

and $Q_-(y)$ and $Q_+(y)$ are the (positive-valued) charge distributions along the electrodes that were solved for in the previous section. In obtaining Equations (33) and (34) we made use of the fact that $\phi_{G-}^* = \phi_{G+}$.

From this point on the evaluation of Equations (29) and (30) for the radiation conductance is relatively straightforward. The integrals in Equations (31) through (34) need to be computed numerically, and explicit forms for P_I and P_{II} need to be substituted in Equations (29) and (30). If only the Fourier component synchronous with the waveguide mode is retained, simple forms for $a_{G+}(x)$ and $a_{G-}(x)$ result. Summing the squared magnitudes of the resultant functions, a_{G+} and a_{G-}, to obtain the power flow, the radiation conductance can be written as

$$G_a(\xi) = G_0 \left| \int_{-3\lambda}^{0} dy \, \phi_{G+}(y) \, Q_-(y) + \int_{-3\lambda}^{\xi} dy \, \phi_{G+}(y) \, Q_+(y) \right|^2 \quad , \tag{35}$$

48

where ξ is the coordinate representing apodization shown in Figure 13. The overlap was given by 3-ξ wavelengths.

Equation (35) has been evaluated numerically for values of ξ between 0 and 1.5 λ. The variation normalized to unity at full overlap is shown in Figure 22 for a Z-cut, Y-point LiNbO$_3$ waveguide. We see that the power input to a transducer drops off rapidly with apodization. By 1.5 λ of apodization the predicted power input is only 33% that at full overlap. Also shown in Figure 22 is the electric potential of the fundamental mode of the waveguide for comparison.

Experimentally obtained center frequency radiation conductances from Figure 16 are also shown on Figure 22. A band along the ξ axis is shown for each apodization because the ends of the apodized electrodes were rounded instead of being terminated rectilinearly, as shown in Figure 13. The two extremes of the band represent the physical ends of the electrodes and the center of curvature of the rounded ends.

Agreement between experiment and theory in Figure 22 is not good. Even with the smallest apodization, $\lambda/4$, the divergence is large. Clearly, either something major has been omitted from the theory, or the conditions believed to be true of the experiment were not, in fact, realized. Many possible explanations have been considered in an effort to remove the discrepancy shown. The first possibility that comes to mind is the omission of charge singularity at the apex of the full length electrode. However, adding a singularity to the data describing the charge at the apex failed to account for the discrepancy. Another possibility we have examined repeatedly is that the waveguide orientation was not Z-cut, Y-point. Yet, all our tests indicated the orientation was correct.
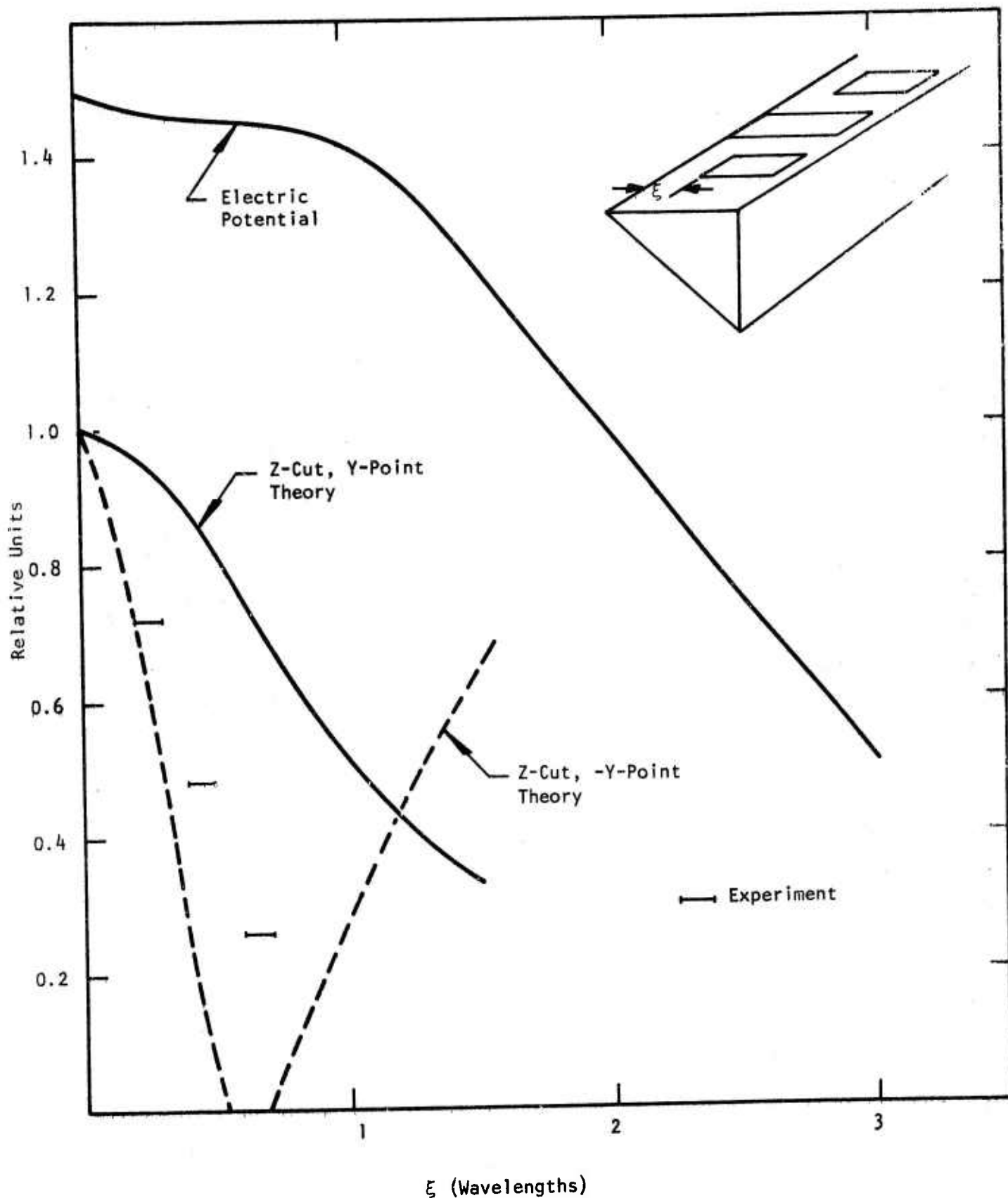
Figure 22 Radiation Conductance Variation as a Function of Apodization for Interdigital Transducers Having a Maximum Possible Overlap of 3.0 λ on a LiNbO₃ Waveguide. The electric potential of the lowest order antisymmetric flexural mode as a function of distance from the apex is also shown for comparison.

The possibility of significant distortion of the normal mode field pattern by the electrodes was examined. Finite element calculations of the field at the surface of the waveguide with and without the top surface shorted showed that the mechanical displacements were essentially identical in both cases (see Figure 14). Mass loading was also considered by comparing results from chrome/gold electrodes to those obtained from chrome/aluminum electrodes. No significant differences were obtained. Finally, the possibility that T_1 in Equation (25) could not reasonably be neglected was considered; however, the question was not resolved.

The conclusion reached is that the radiation conductance falls off much more rapidly than would be desired. This puts stringent demands on transducer fabrication tolerances if weighting must be employed. Because of the current divergence between experiment and theory, the controlling factors on the electrode tap strength have still not been identified. A quantitative theory needs to be perfected before control over band shaping can be applied.

SECTION III

ETCHING STUDIES

A. Introduction

Waveguide fabrication in $LiNbO_3$ and α-quartz is carried out by etching the materials in boiling concentrated hydrofluoric acid. Wafers of the materials are carefully SYTON polished on one surface and then coated with sputtered chrome and gold. Etch windows that define the waveguide apex are opened in the protective metals to expose the crystal between waveguides. Etching is then carried out in a large volume of boiling HF without mechanical agitation. Etch rates are about 40 μm/hour and 6 μm/hour on ST-cut quartz and +Y-cut $LiNbO_3$, respectively.

Two major difficulties limit success in the fabrication of the waveguides. One problem is that the protective metals do not adhere sufficiently well to the substrates and lift off during the etching process. This problem is con-siderably worse for quartz than for $LiNbO_3$. The second major problem is crystal defects which etch differently from the major lattice. This problem has been worse for $LiNbO_3$ than for quartz. The crystal defect problem in quartz is significant only when attempts are made to etch large (~ 0.003 inch) waveguides. Because of the considerable difficulties presented by the defects in $LiNbO_3$ and our interest in the higher coupling material, we have devoted a major portion of our effort to examination of the $LiNbO_3$ crystal defects.

B. Etching of $LiNbO_3$

1. Crystal Axes Polarity of $LiNbO_3$ Plates

Before etching waveguides in $LiNbO_3$ plates can be attempted, the orientation of the crystal axes must be determined. We have found that X-directed waveguides can be etched only on the +Y surface of Y-cut wafers and that those waveguides will be oriented with the apexes pointing toward the -Z direction. Consequently, the +Y surface must be identified for wafer polishing

and the -Z direction located for photomask orientation. These surfaces can be readily identified by using hydrofluoric acid as an etchant, since they manifest distinctly different appearances after etching.

Y-axis polarity of Y-cut LiNbO$_3$ wafers can usually be determined from the sawed wafer before etching. On the basis of observations made on Y-cut wafers obtained from several different saws, two different vendors, and three different growth directions, the following generalizations have been found to hold.

+Y-Face

This face has a "flowed" appearance and seems to show saw marks. It has a higher sheen, and the sheen is streaked. At 200X one can see what appears to be regular periodic scratches covered by a thin layer of LiNbO$_3$ crumbs. This face becomes negative when Y-axis compression is applied.

-Y-Face

This face appears dull, matte, and uniform. At 200X it appears to have scratches also, but it is covered by a thick layer of large LiNbO$_3$ crumbs. This face becomes positive when Y-axis compression is applied.

Comparative photographs at ∿ 500X of the as-sawed Y-faces are shown in Figure 23. The faces have quite different appearances and are easily distinguished. Figure 24 shows the Y-faces at ∿ 500X after etching for about two hours in boiling concentrated hydrofluoric acid. The apparent differences in the etched surfaces are even greater when they are viewed through the microscope than the photographs suggest.

Determination of the Z-axis polarity can also be made by hydrofluoric acid etching. In this case, however, standard laboratory microscopes are not
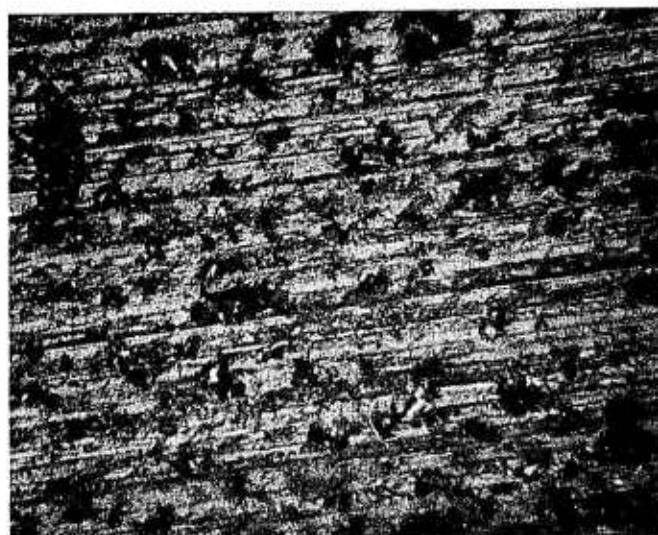
Figure 23 Y-Surfaces of a LiNbO$_3$ Wafer at ~ 500X.
Note the difference in appearance of the
+Y face (bottom photo) and the -Y face (top
photo) of the wafer after it was sawed from
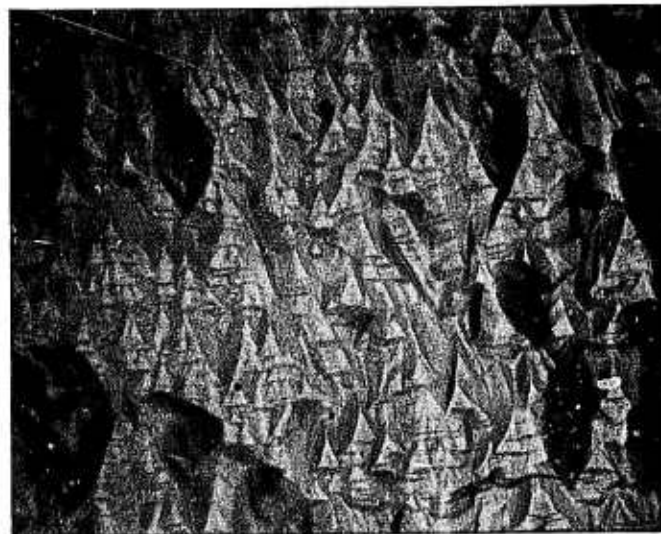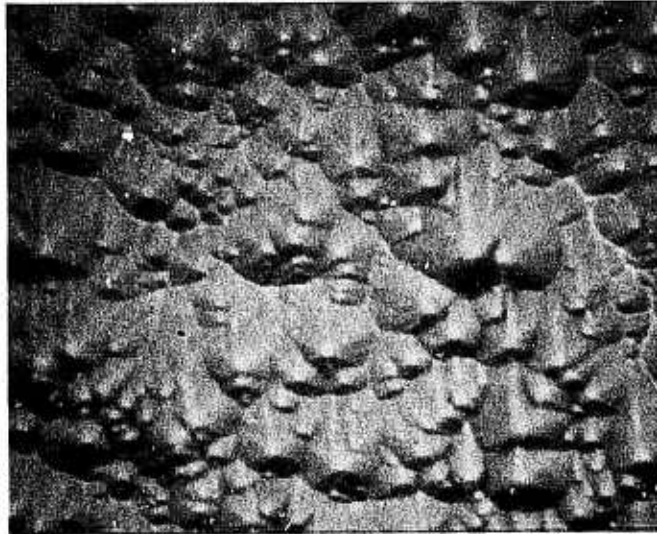a boule.

54

Figure 24 Y-Surfaces of a LiNbO₃ Wafer After Etching for
          About Two Hours in Boiling Concentrated HF.
          Top photograph shows the -Y face, bottom
          photograph the +Y face. Magnification ~ 500X.

adequate to see the high texture of the surface, and unlike that of the Y-faces, the appearance of the +Z-face tends to be dependent on the prior processing of the surface.

Figure 25 shows +Z and -Z faces of $LiNbO_3$ after etching in boiling concentrated hydrofluoric acid. The general appearance of the -Z face at $\sim$ 500X after etching for two hours is distinguishable. However, the depth of field of the microscope is not capable of bringing the entire picture into focus.

The two illustrations in Figure 25 of the +Z face show the difference prior processing makes in the appearance of the surface. The upper photograph shows the result after two hours of etching of the Z-flat of a (yz) $LiNbO_3$ plate as supplied by the vendor. That surface was then lapped in the X-direction only using 20 μm grit until it was completely roughened. It was then etched for another four hours to produce the appearance shown in the lower photograph. Polished +Z surfaces that are etched in boiling HF also have the appearance shown in the lower photograph of Figure 25.

SEM photographs of the ±Z surfaces illustrated in Figure 25 are shown in Figure 26.

From this series of photographs, laboratory identification of the polarity of $LiNbO_3$ axes can readily be carried out. This should be of value not only in waveguide etching, but also in selecting a particular surface for wafer polishing.
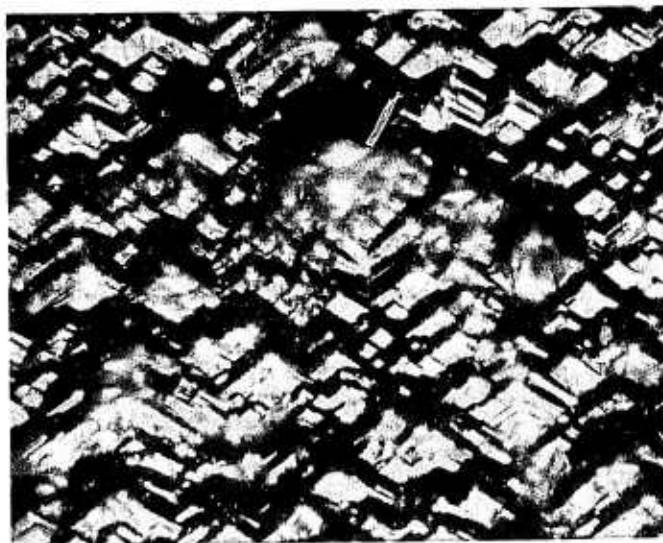
2. $\underline{LiNbO_3}$ $\underline{Etch\ Plane}$

The plane of $LiNbO_3$ we have attempted to use as the lower face of the wedge waveguide is approximately (20 · $\bar{3}$). As illustrated in Figure 27, it is parallel to the X-axis and down $\sim$ 26° from the Y-plane. The 26° angle was

-Y

±Y

±Y
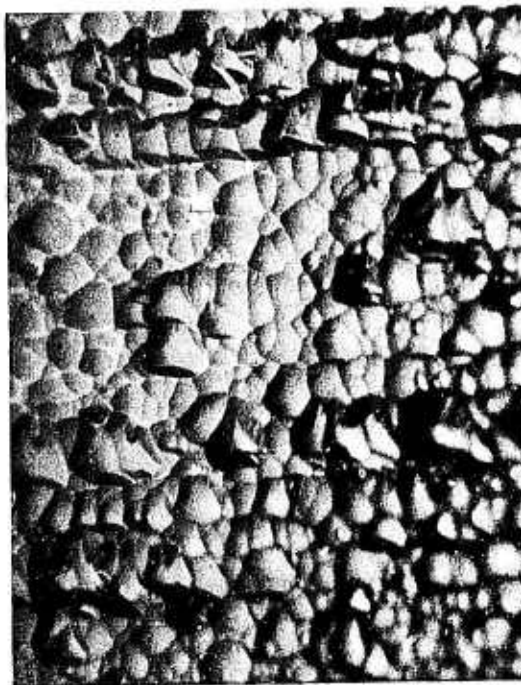
Figure 25 Z-Surfaces of LiNbO$_3$ After Etching in Boiling Concentrated HF.
Magnification ~ 500X. Left-hand photograph shows the -Z face
after two hours of etching. Upper right-hand photograph shows
the +Z flat on a wafer after two hours of etching. Bottom
right-hand photograph shows the same +Z surface after roughening
in the +X direction only and etching for another four hours.

57

±Y
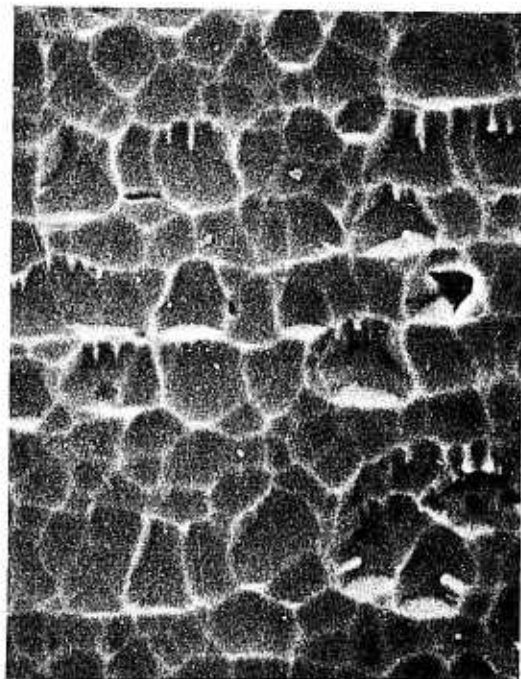
±Y
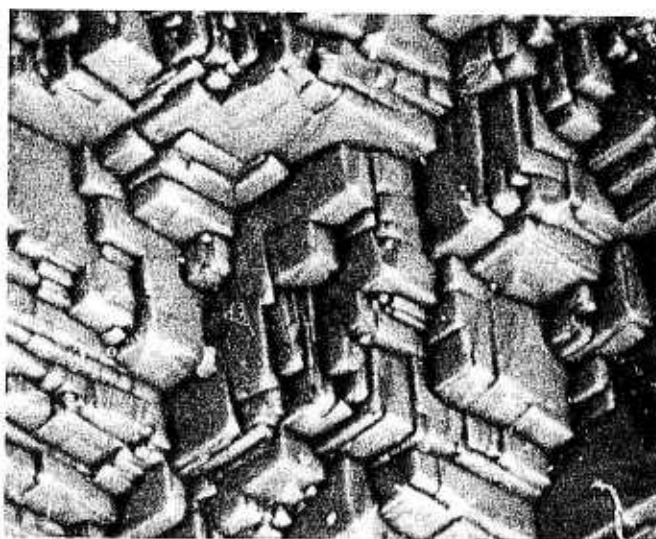
±Y

Figure 26 Scanning Electron Microscope Photographs of the Surfaces
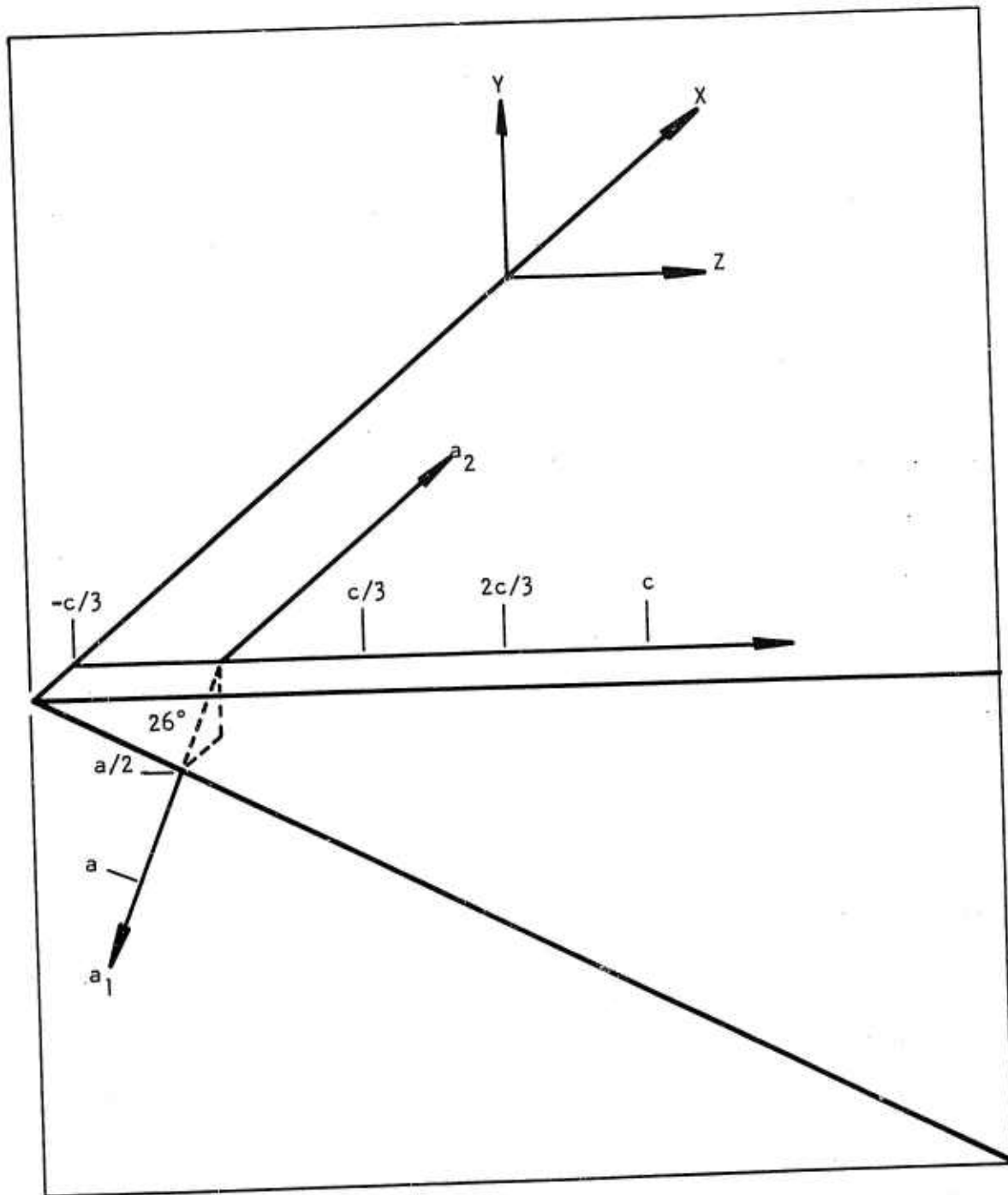Shown and Described in Figure 25

Figure 27 Schematic Representation of LiNbO₃ Waveguide
Showing Both Rectangular and Hexagonal Axes.
The lower surface of the waveguide is
approximately (20 · 3̄).

determined empirically from multiple etching experiments. Calculations taking into account the unit cell dimensions, $a = 5.1483$ Å, $c = 13.863$ Å, and the 26° angle, give hexagonal lattice parameters of $(1.978 \quad 0 \cdot \bar{3})$, which we have rounded to the values quoted above.

3. $LiNbO_3$ Waveguide Results

Our results on acoustic quality Y-cut $LiNbO_3$ have been uniformly discouraging. In general, we find that the crystals have very defective lattices, and the extent of their deviation from single-crystal is more than enough to prevent etching uniform waveguides. Optical parametric oscillator quality $LiNbO_3$ has also been examined. While the defects present in this quality of $LiNbO_3$ are considerably less than those present in the acoustic-grade LiNbO3, there are still far too many to achieve a significant propagation length.

Figure 28 shows a $LiNbO_3$ waveguide cross section. The under-surface of the waveguide is single-faceted and the apex is extremly sharp at the plane where the waveguide was cross-sectioned. However, this geometry cannot be maintained over an appreciable propagation distance. Figure 29 shows how severe the waveguide uniformity problem can be. In this photograph the viewing angle is $\sim 10°$ up from the plane of the wafer and the waveguides recede from view. Apex roughness is extreme and appears to be without characteristic form. That, however, is a consequence of the viewing angle. Under careful examination, the irregularities in the apex show a definite faceting. Also consider that relative to the apex of the guide, the back edge (upper surface) of the guide is quite uniform. Because of the quality of the back edge, it seems unlikely that irregular etch mask erosion is responsible for the waveguide nonuniformity.

The mosaic photograph in Figure 30 is a top view of the waveguides shown in Figure 29. Light regions in the illustration are the top surfaces
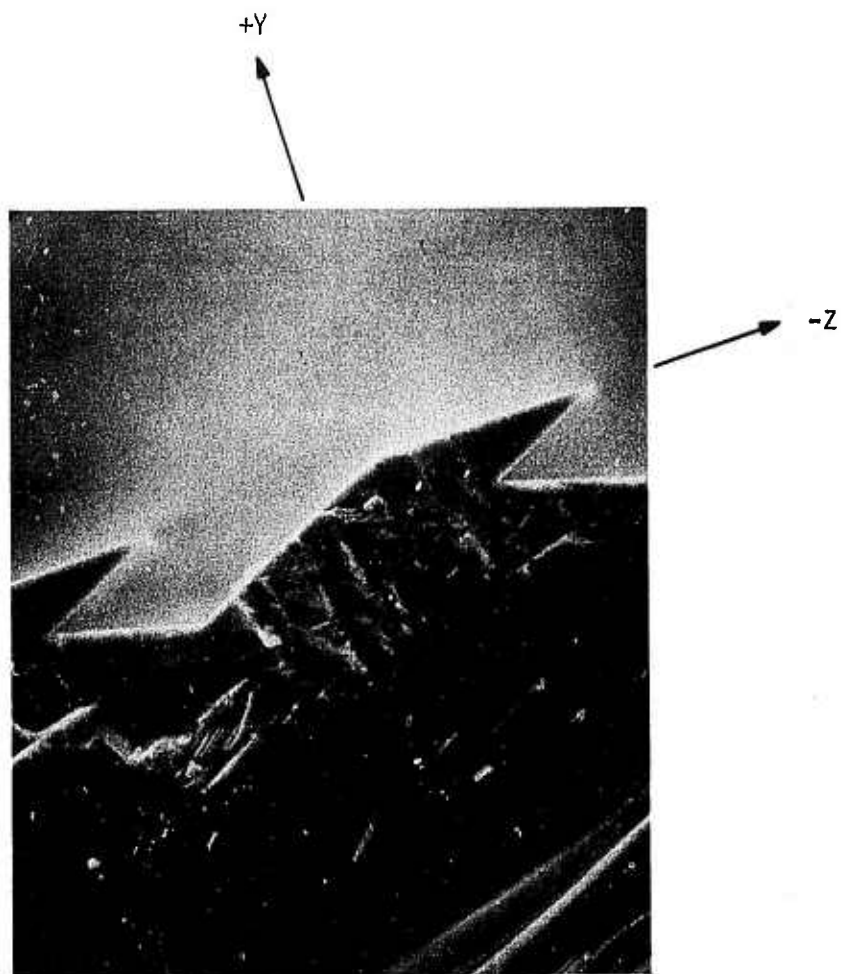
+Y

−Z

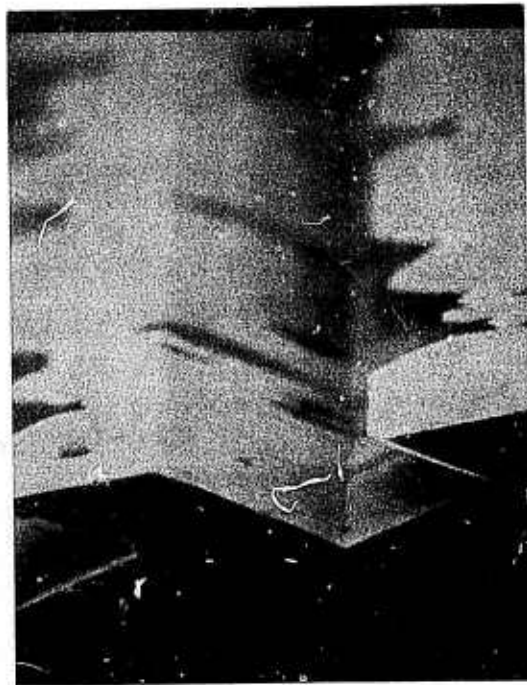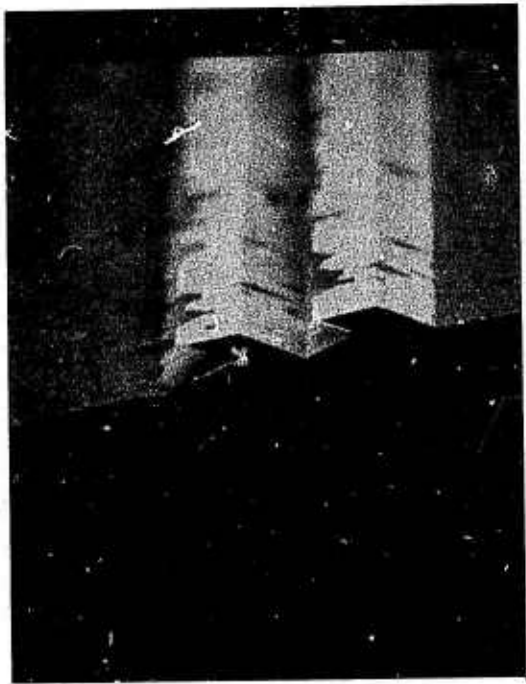Figure 28   Etched LiNbO$_3$ Waveguides.   Cross-sectional view at $\sim$ 800X.

61

Figure 29 Two Etched LiNbO$_3$ Waveguides. Perspective views at $\sim$ 290X and 740X on the left- and right-hand sides, respectively.
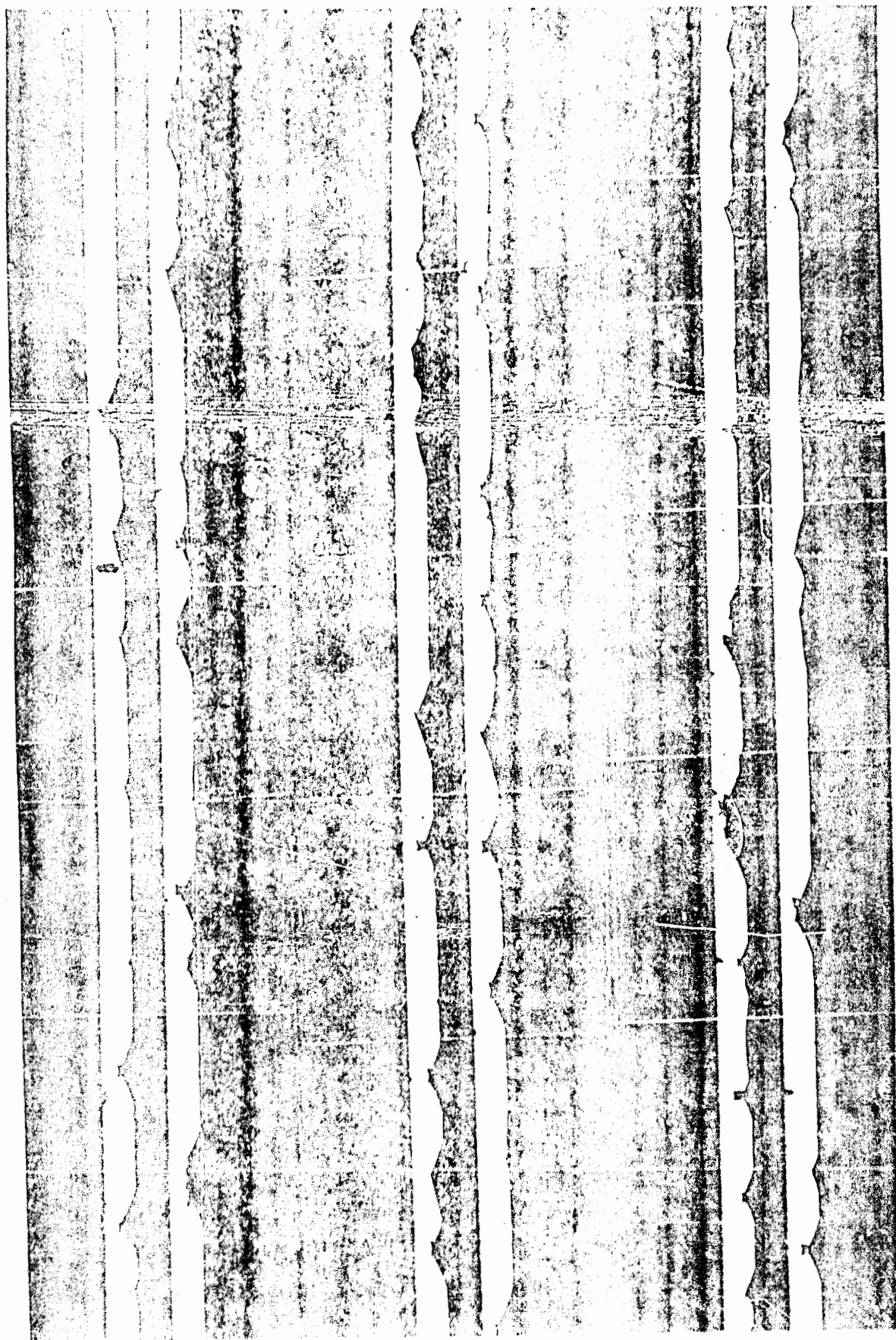
Figure 35 View at 150X into the Y-Surface of Etched Lining Waveguides.
The irregular lines are the scored margins of the regions.

of the waveguides, and dark regions have been etched down from the original wafer surface. The undercut edge is the lower side in all of the six waveguides. Now the faceting of the waveguide discontinuities is evident, and in a number of cases the problems can be traced from waveguide to adjacent waveguide. Again note that the top line of the waveguide upper surface (the edge not undercut) is relatively uniform.

The particular type of problem illustrated in Figure 30 is most likely due to inclusions in the material. If the wafer is tilted so that the viewing angle is as shown in the inset in Figure 31, then one sees faceted etch pits. These pits tend to correlate to the apex defects. The defect density varies from wafer to wafer, but in no case has this type of defect had a negligible density.

Polishing damage produces a different type of apex interruption. The photographs in Figure 32 illustrate what is thought to be damage due to subsurface microcracks induced during wafer grinding and polishing. Light regions in the photographs are the tops of the waveguides, and dark regions are the etched spaces between waveguides. The V-shaped indentations occur on the apex side of the waveguide and in some cases etch through to the other side of the waveguide. In the lower photograph some of the loci of defects move out of the field of waveguides into the unetched portion of the wafer. No visible crystal damage can be detected in the unetched crystal along the loci extrapolations or on the waveguide top surfaces, yet the damage is certainly present, as the etchant reveals. Note that the indentations in Figure 32 are V-shaped and point along the defect locus, whereas the faceted defects in Figure 30 have a definite Z-axis orientation.

Another characteristic defect observed in the $LiNbO_3$ waveguides is shown in Figure 33. In this photograph the waveguides are the light regions, and the dark regions are the etched portion of the surface. The undercut edge
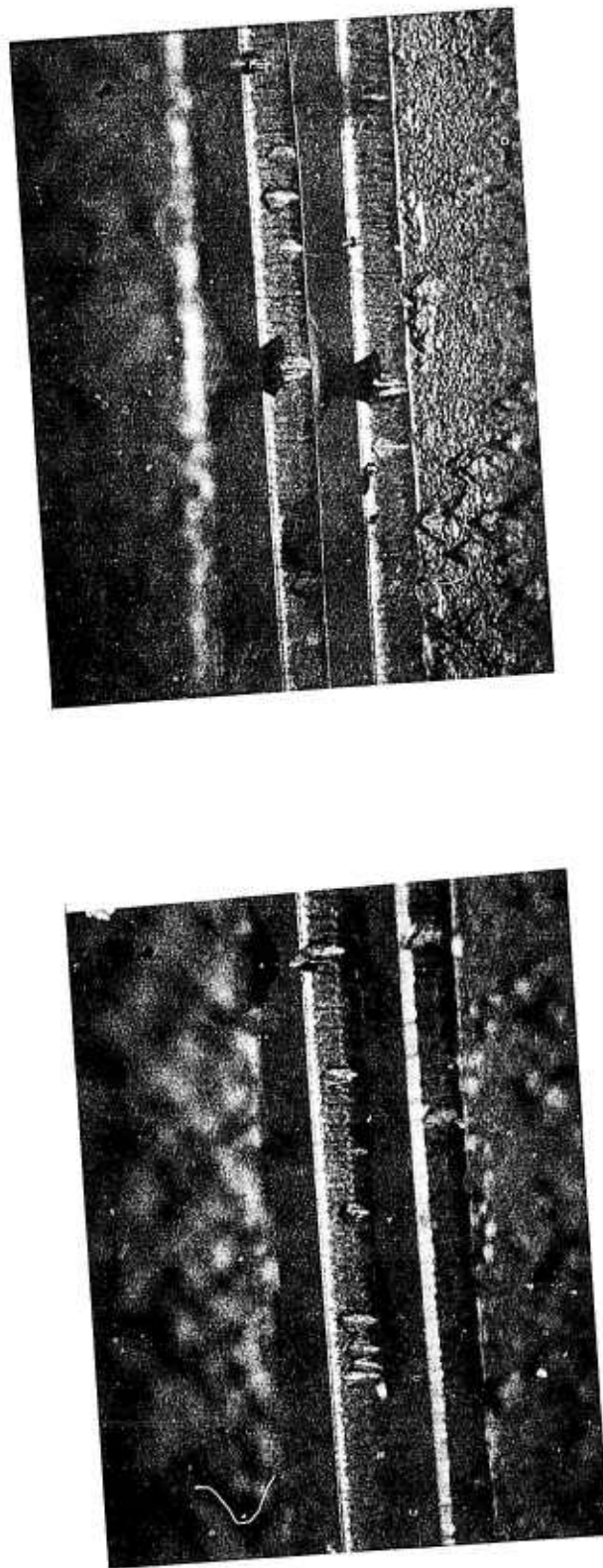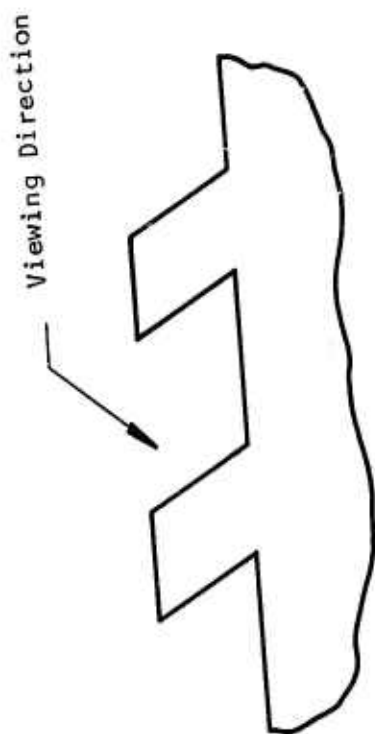
Viewing Direction
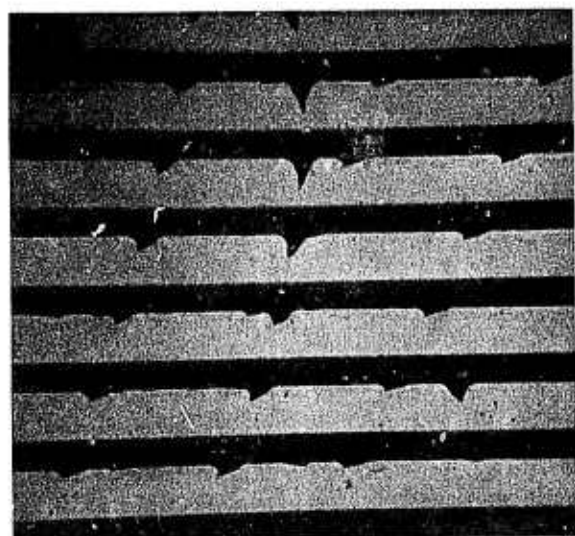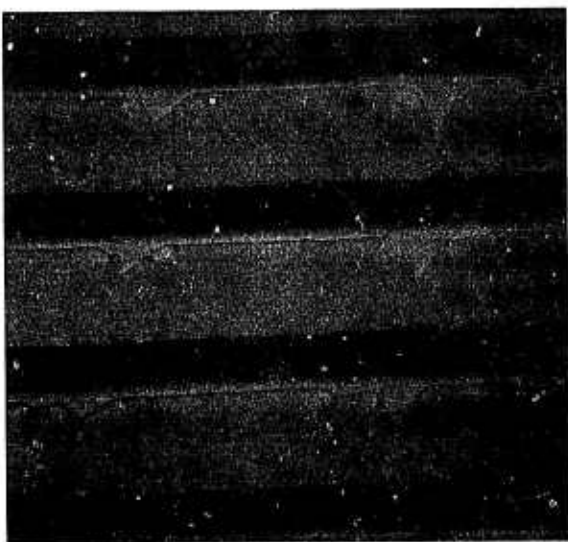
Figure 31 Etch Pits on the Side Wall of LiNbO₃ Waveguides. ~ 100X.

Figure 32 Polishing Damage in a Field of Etched LiNbO₃ Waveguides. Lower photograph at ~ 100X. Upper left- and right-hand photographs at ~250X and ~ 500 X, respectively.
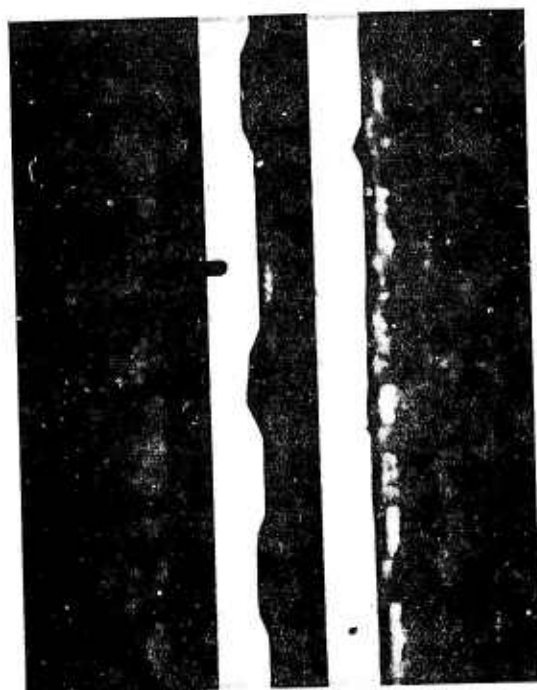
Figure 33 Etched LiNbO$_3$ Waveguides Showing Characteristic Indentations of Apex Line. Magnifications are ∼ 50X and 100X in the left- and right-hand photographs, respectively.

is the lower edge in the photographs. Note that the waveguide apex has three faceted indentations. The apex line recedes from the etch mask edge at a shallow angle and then again runs approximately parallel to its original course before returning along another shallow-angled facet. The angle of these facets correlates well to a line structure that can be revealed in the Y-face of the wafer by etching with a 60:40 mixture by volume of H_2SO_4 and H_2O_2.

Figure 34 shows photographs of apex irregularities that correlate to a line structure on the Y-surface of the wafer. In this case the waveguide extends upward from the bottom of the photograph. Figures 34(a) through 34(c), which are a series of photographs of the same region at $\sim$ 200X, $\sim$ 500X, and $\sim$ 1000X, show clearly that the apex defects indent from the line of the etch mask to specific planes of the crystal.

On the top surface of the waveguide one can see a line pattern that terminates at the corners of the indentations in the waveguide apex. This effect is most pronounced in Figure 34(d) ($\sim$ 1000X), where the defect was caused by either a scratch or an inclusion. What these lines are still has not been determined. We know that they are always present in the $LiNbO_3$ and that they correlate to demarcations in the etch characteristics of the crystal lattice. Also, they always have one of two characteristic appearances: they either are oriented at the shallow angle to the X-axis as shown in Figure 34, or they are exactly X-directed. Sometimes both orientations occur on the same wafer.

In an effort to determine if the line pattern was associated with volume effects within the crystal or was basically a short-range or surface effect, a 0.020 inch wafer of $LiNbO_3$ was polished on both +Y and -Y faces and etched in the $H_2SO_4:H_2O_2$ solution. After the line pattern was evident on the surfaces, gold was evaporated on the two faces and then etched, leaving 0.080 inch x 0.080 inch squares on each face. The squares on the two faces were so
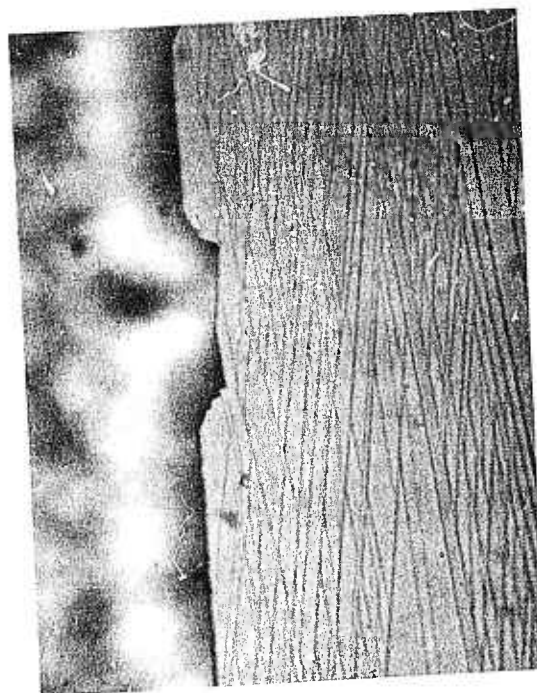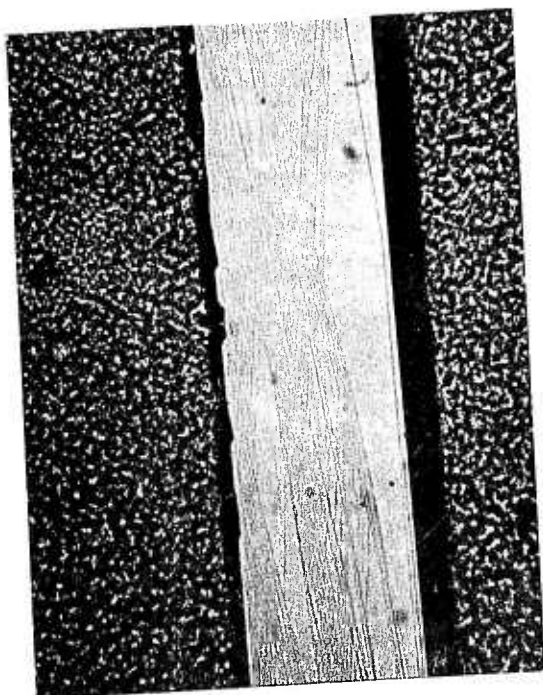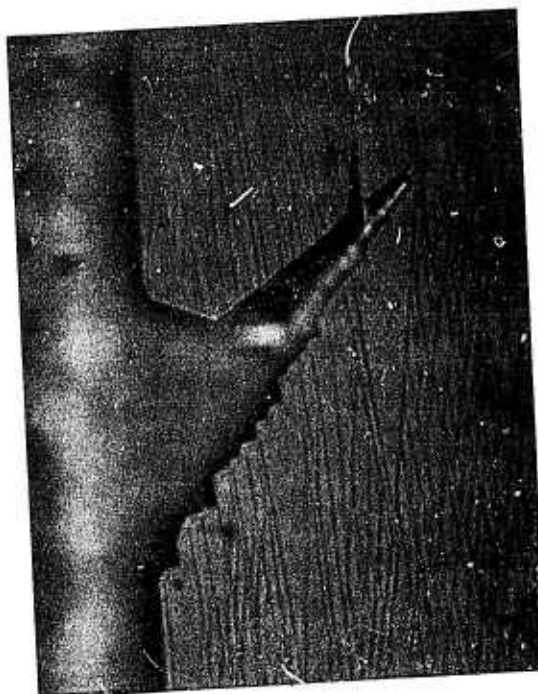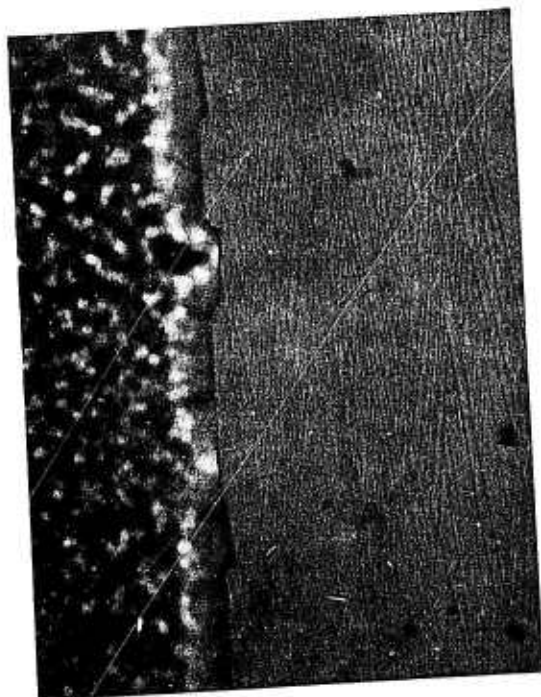
Figure 34 Correlation of Apex Defects With Y-Surface Line Structure. Magnifications clockwise from upper left-hand corner are ~ 200X, ~500X, ~ 1000X, and ~ 1000X.

arranged that the pattern on one face corresponded to a translation of the pattern from the other. With the two arrays of gold squares to serve as relative coordinates, one could examine the wafer to see if any effects could be traced through the 0.020 inch thick wafer.

Figures 35 and 36 illustrate the line structure on the two faces. The squares in the photographs are 0.080 inch by 0.080 inch, and illumination of the samples was from either the right- or the left-hand side at about 30° from the plane of the wafer. Taly-Step and SEM information indicates that the lines evident in the figures are on the order of 50 Å removed from the average plane of the wafer. When illuminated at normal incidence, the lines are virtually undetectable visually.

The features in Figures 35 and 36 can be divided into two classes, those that are in focus and those that are not. The in-focus features are on the top side of the wafer, while the out-of-focus features are on the other side and are being seen through the $LiNbO_3$. The ability to see features through the wafer gives further registration of the two surfaces and allows one to look carefully for effects that track through the wafer. Even though there are a large number of features on the two surfaces, we cannot find one field of lines that truly tracks through the wafer. The effects either are localized volume effects with less than 0.010 inch range or are a consequence of surface preparation with less than 0.020 inch penetration.

C. Etching of α-Quartz

1. Quartz Etch Plane

Most of the work on quartz etching has been performed on ST-cut wafers. High-quality waveguide geometries are readily obtainable by etching this surface, once surface polishing and etch mask preparation difficulties have been overcome. However, the waveguide size must be limited to ∿ 0.001 inch to avoid crystal defect problems and erosion of the etch mask.

70

Figure 35 Y-Surface of LiNbO$_3$ Wafer. The 0.020 inch thick wafer was polished on both sides, etched to reveal the line structure shown, and had 0.080 inch x 0.080 inch registration squares defined on the two surfaces.
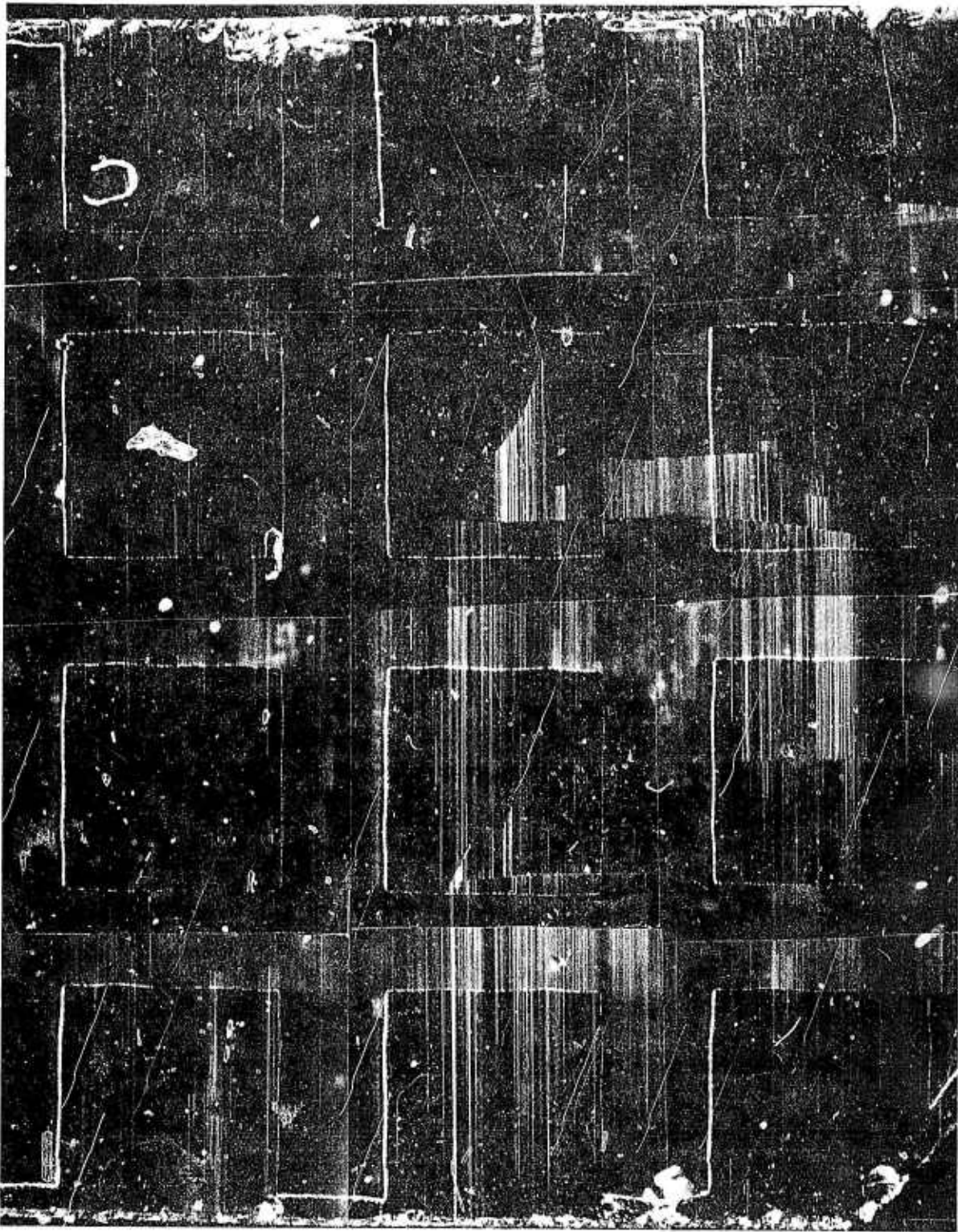
71

Figure 36   Y-Surface of LiNbO$_3$ Wafer.   This is the surface opposite that
shown in Figure 35.

We have etched many waveguides on ST-cut quartz wafers with orientations near that shown in Figure 37 and have found several minor etch planes in addition to the major slow etch plane that defines the lower edge of the waveguide. The presence of these other planes is sensitive to the exact angle of orientation of the waveguide. There is an angle at approximately 10° off X where the lower surface of the guide is a single plane. At ±1° from this direction in the plane of an ST-cut wafer, the lower guide surface became multifaceted.

Figure 38 shows a perspective view of pairs of waveguides on ST-cut quartz. The waveguides are approximately 25 μm high; their lower surfaces are single-faceted, and the apexes are smooth over large propagation lengths. Top angles of these waveguides measured about 60°.

The waveguides were formed by etching in boiling HF for approximately one hour with the surface masked by a chrome-gold pattern. Etch mask erosion was minimal, and defects in the chrome-gold mask were rare, as evidenced by the uniformity of the waveguides.

2. α-Quartz Crystal Defects

The waveguides shown in Figure 37 have defect-free propagation distances on the order of 0.500 inch or more. Achieving that quality of result when the size of the waveguides is increased from 0.001 inch to 0.003 inch has proved to be a challenge. First, the metallizations on the quartz do not withstand the HF etch. Second, the longer etch times reveal crystal defects in the quartz that are not significant in the smaller guides.

The defects in quartz appear to be line defects that radiate out from the seed of the boule. The HF preferentially attacks these points on the unpolished side of the wafer and etches through to the waveguide side in a short time (∿ 30 minutes). If the etch times are long, as required for large
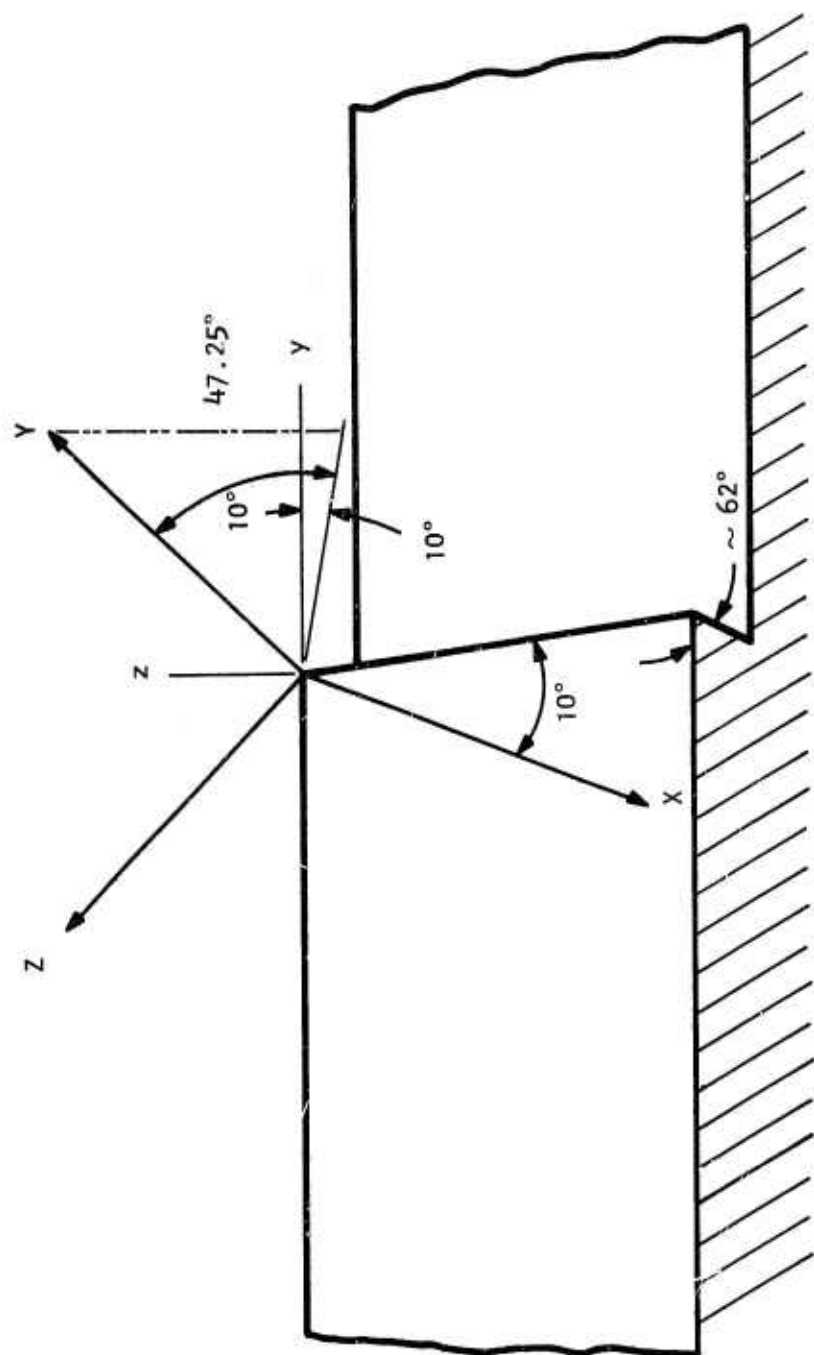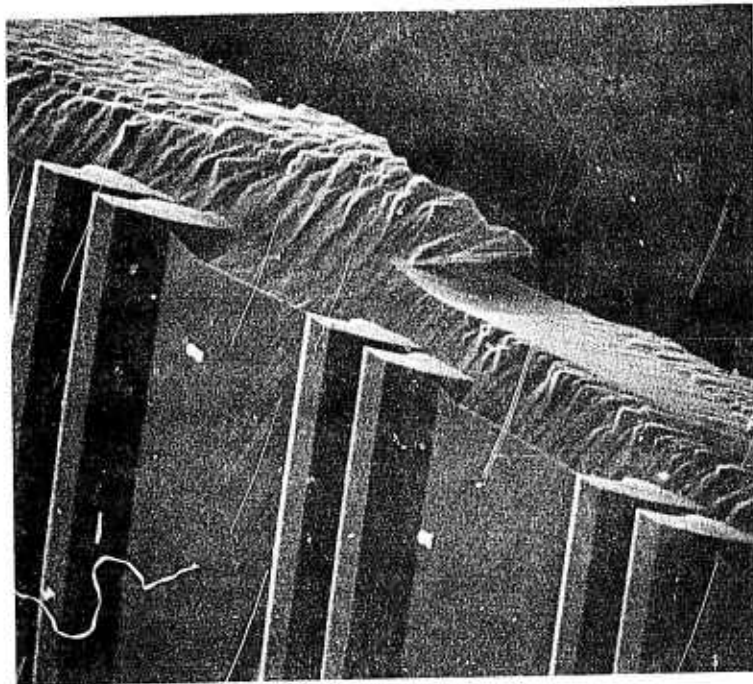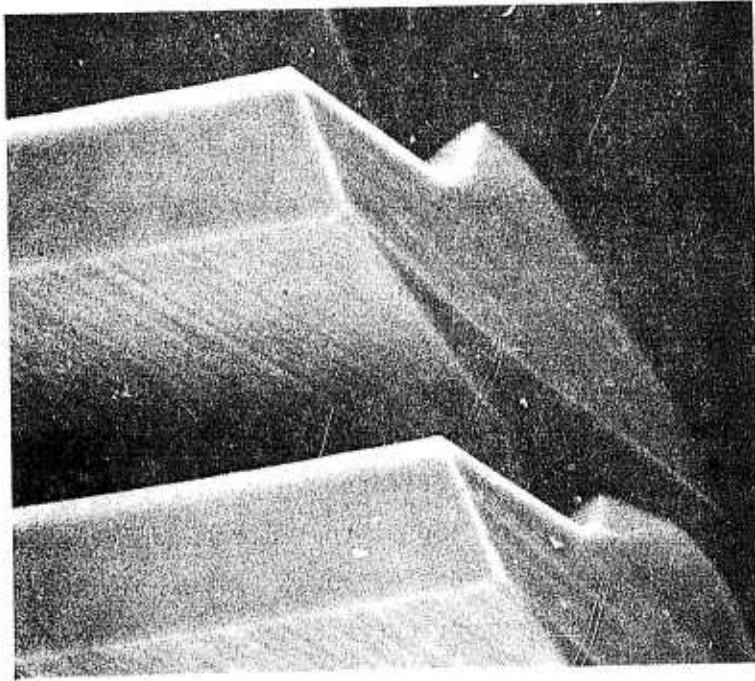
73

Figure 37 Orientation of an Etched Ledge on ST-Cut Quartz

74

(b)

(a)

Figure 38   Waveguides Etched in ST-Cut Quartz.   The top angles are 60°.
(a) 150X; (b) 700X.

75

waveguides, the diameters of the line defects that permeate the crystal become large enough to disrupt the waveguides.

Figure 39 shows a sequence of four through-focus photographs of the line defects observed in quartz. The major light area is the upper surface of the crystal that was protected by the metals. The gray band is the overhanging waveguide which extends downward. Magnification is $\sim$ 100X, and moving from the upper left-hand corner clockwise, the focus is adjusted from the top of the wafer to the bottom. The line of the defects, which etched through from the back of the wafer to emerge at the top of the wafer under the chrome/gold, can be traced through the sequence of photographs. Figure 40 shows the same type of sequence at $\sim$ 200X. Again, starting at the upper left-hand corner photograph and moving clockwise, the focus moves from the top of the crystal to the bottom.

3. Other Etchants and Etch Masks for Quartz

Because of the high rate of attack of HF on chrome/gold films on quartz, other etch masks and other etchants were examined. The other etch masks that were used with HF were sputtered molybdenum, sputtered molybdenum/gold, sputtered titanium/gold, and evaporated silicon. None of these films provided better protection than the sputtered chrome/gold films.

Two fluxes were also tried as etchants for quartz. The etch mask was sputtered chrome/gold in both cases. The first system was NaOH-KOH. A 50:50 Mol.% mixture of the two hydroxides liquefies at $\sim$ 170°C, and etching was carried out at just above the melting temperature. The substrates were ST-cut quartz patterned at various angles to see if orientation-dependent etching occurred anywhere on the plane.

We found that after only 12 minutes of etching, the chrome/gold film began to lift from the substrate. In addition, the etchant showed no

Figure 39 Waveguides on ST-Cut Quartz. Magnification is ~ 100X. The gray band below the major white region is the overhanging waveguide. Moving clockwise from the upper left-hand corner, the focus moves from the top of the crystal to the bottom. The course of defects through the crystal can be seen.
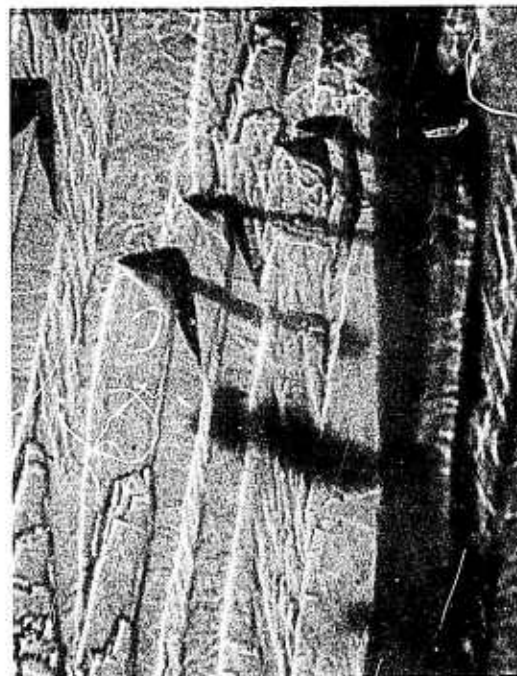
Figure 40 Waveguides on ST-Cut Quartz. A sequence of photographs like that in Figure 39, except at ~ 200X.

orientational preferences, but instead etched essentially isotropically. The etch rate was extremely high, approximately 0.050 inch per hour.

Because Li_2CO_3 and K_2CO_3, in theory, do not attack chrome, we tried a 50:50 by weight mixture of these two materials as an etchant. Unfortunately, this combination will not liquefy until the temperature reaches $\sim$ 500°C. Care must be taken in etching quartz at temperatures above 500°C because of the quartz phase change at 573°C. In the case of the carbonate mixture used here, however, the temperature problem is not a limiting factor, since the flux lifted the chrome/gold film from the substrate. We presume that impurities in the carbonates are responsible for etching the chrome. Once again, no preferential etching was detected.

SECTION IV

CONCLUSIONS

A. Waveguide Fabrication

In both quartz and LiNbO$_3$ crystal defects are a severe limitation to acceptable waveguide formation, and in LiNbO$_3$ they are the most important limitation. The defect density is sufficiently high that the longest propagation length between defects is measured in tens of mils. Erosion of the chrome/gold etch mask on LiNbO$_3$ is no longer considered a major problem, now that a rigorous SYTON polishing procedure has been adopted.

Quartz not only has crystal defects, but also presents an etch mask erosion problem that was not solved by improved polishing procedures. Should the mask erosion problem be overcome, it is conceivable that very high frequency, rather than low frequency, waveguides could be etched in quartz. The reason for the high frequency limitation is that long etch times reveal line defects in the quartz which disrupt the waveguides. However waveguides limited to high frequencies ($\lambda \sim 10$ μm) would necessitate the development of techniques for the fabrication of very fine geometry metallizations at the apex of the waveguide.

B. Transducer Fabrication

In the work reported here we have concentrated on the sensitivity of the transducers' electrical characteristics to variation in the metallization produced. As might be expected from the fact that the transducers are very small (essentially a collection of end effects), the sensitivity we observed was considerable. We examined transducer apodization as a method of weighting with the thought that it might be reasonably insensitive to fabrication errors. However, the results showed that the coupling dropped off so rapidly with apodization that in only 1/2 λ of electrode length variation, the coupling could be varied from 100% to only 40% of full coupling. This means that the effective weighting range still would require precise control of electrode

lengths at the edge of a planar surface, a severe requirement for commonly used photolithographic processes.

Another major problem of transducer fabrication is to develop an electrode configuration capable of achieving high coupling. We have ignored this problem entirely by working at low frequencies where the electrodes could be individually bonded to achieve an interdigital polarity sequence. Known techniques for fabricating bus bars with air gap crossovers could be employed here; however, the amount of substrate taken up by the pads increases the size of the component to the point where the waveguide must provide a function not achievable with other devices in order to be competitive.

Grating mode configurations for the transducer, where the underside of the wedge is completely metallized and grounded, provide a potentially feasible solution. Once again, though, metallizations must be controlled at a corner. In this case the metal on both sides of the corner affects the results. Additionally, this method even more than the interdigital approach, is highly vulnerable to spurious mode problems.

Finally, there is a wide variety of mode conversion schemes, many of which work. However, all require so much additional substrate that unless the waveguide provides a unique signal processing function, it is inferior to other device alternatives.

C.   Future Work

Additional work can profitably be performed to help move toward a workable acoustic waveguide embodiment. Specific examples include: (1) A study of quartz polishing and etchant-resistant films in order to achieve large-dimension waveguides. (Quartz manufacturers report that defect-free quartz can be obtained.) (2) A study of $LiNbO_3$ growth processes in order to achieve a low defect density. (3) Examination of other substrate media for their orientation-dependent etching properties.

ACKNOWLEDGMENT

REFERENCES

1. P. Lagasse, "Finite Element Analysis of Piezoelectric Elastic Waveguides," IEEE Trans. Sonics Ultrason. SU-20, 354 (1973).

2. I. Mason, M. Motz, and J. Chambers, "Parametric Interaction of Acoustic Surface Wedge Waves," Electron. Lett. 8, 429 (1972).

3. I. Mason, R. DeLaRue, R. Schmidt, and E. Ash, "Ridge Guides for Acoustic Surface Waves," Electron. Lett. 7, 395 (1971).

4. R. Rosenfeld and K. Bean, "Fabrication of Topographical Ridge Guides on Silicon for VHF Operation," Proc. IEEE Ultrasonics Symposium, p. 186 (1972).

5. R. Wagers and D. Weirauch, "Acoustic Waveguides Formed by Orientation Dependent Etching," Proc. IEEE Ultrasonics Symposium, p. 539 (1975).

6. D. Weirauch, "The Correlation of the Anisotropic Etching of Single Crystal Silicon Spheres and Wafers," J. Appl. Phys. 46, 1478 (1975).

7. P. Lagasse, I. Mason, and E. Ash, "Acoustic Surface Waveguides - Analysis and Assessment," IEEE Trans. Microwave Theory Tech. MTT-24, 225 (1973).

8. G. Kino and R. Wagers, "Theory of Interdigital Couplers on Nonpiezoelectric Substrates," J. Appl. Phys. 44, 1480 (1973).

9. B. Auld, Acoustic Fields and Waves in Solids (Wiley-Interscience, New York, 1973), Vol. II, p. 161.